Characterization of semiconductors from photoconductivity techniques: Uniform and monochromatic illumination

Christophe Longeaud, Javier Schmidt, Jean-Paul Kleider

2

Characterization of semiconductors from photoconductivity techniques: Uniform and monochromatic illumination

Christophe Longeaud[1], Javier Schmidt[2] and Jean-Paul Kleider[1]

[1] Group of Electrical Engineering – Paris (GeePs), CNRS, CentraleSupelec, Université Paris-Saclay, Sorbonne Université, 11 rue Joliot Curie, 91190 Gif sur Yvette, France

[2] Instituto de Física del Litoral (IFIS–Litoral), CONICET-UNL, Güemes 3450, S3000GNL Santa Fe, Argentina

Abstract

In this chapter we present characterization techniques based on the uniform illumination of photoconductive semiconductors with monochromatic light. Among these techniques, one is the well-known steady-state photoconductivity (SSPC) experiment. Under these conditions of illumination, a power law dependence of the photoconductivity σ with the DC generation rate G_{dc} is usually observed: $\sigma \propto G_{dc}^{\gamma}$. Starting from the transport equations we demonstrate that the information contained in σ and in the coefficient γ offer the possibility to achieve a spectroscopy of the band gap states of the studied semiconductor. We illustrate this result by means of numerical calculations and experimental results. We also present another experiment, based on the same type of illumination, but for which the flux is modulated at different frequencies: the modulated photocurrent (MPC) technique. The theoretical developments based on the solution of the transport equations show that two regimes can be defined: the low frequency regime and the high frequency regime. After defining these regimes, we show that a gap states spectroscopy can be achieved in each regime. All these developments are emphasized by numerical calculations and illustrated with experimental results. Finally, we show that SSPC and MPC bring complementary information on the studied semiconductor to obtain a rather complete overview of the gap states distribution and of the transport parameters such as carrier mobility capture coefficients of the trapping states.

Keywords: photoconductivity, steady-state photocurrent, modulated photocurrent, density of states, transport parameters

2.1. Introduction

The knowledge of the density of states (DOS) in the gap of semiconductors is of primary importance since these states partially control the optoelectronic properties of these materials. Semiconductors are present in a wide range of applications, such as absorbers in photovoltaic devices, but also for high power electronics (SiC), memories (GeTe, GeSnTe), and photorefractive components (BTO, CdTe), to quote some of them. Depending on the targeted application, the DOS must be either as low as possible to minimize recombination, or tailored during the fabrication process to obtain a precise function. To investigate on this DOS and optimize the fabrication process, advanced characterization techniques have been proposed, many of them based on the photoconductivity properties of the material. Basic aspects of photoconductivity have been treated in the classical works of R. Bube [1, 2], S. Ryvkin [3] and A. Rose [4]. An introduction to several photoconductivity-based techniques has been given in a recent publication by S. Reynolds [5].

In this work we shall present some of the most powerful techniques developed for the characterization of photoconductors. After presenting briefly the conditions under which each experiment is performed, we shall describe the information gained with each technique, as well as its advantages and drawbacks. We shall also underline that some experiments are complementary, either because they are sensitive to different transport parameters or because their combined use brings information on peculiar properties that could not be revealed if the techniques were employed separately.

For all the experiments described in the following the samples are built in coplanar geometry. For this purpose, two electrodes forming ohmic contacts, 0.5 to 1 cm long and 1 to 2 mm apart, are deposited on top of or below the materials under study. A steady bias is applied between these electrodes and the current resulting from the light generation is collected, amplified and treated to extract as much information as possible.

This information largely depends on the type of illumination shone onto the sample. This illumination can be uniform in between the electrodes or can be regularly distributed, as in the case of interference fringes parallel to the electrodes. In addition, one can play with the wavelength of the light to gain insight into the materials properties. In most of the experiments, the light is monochromatic with photon energy larger than the band gap of the studied material. In this case, the wavelength and/or the material thickness are chosen such that the light is as much as possible uniformly absorbed in the depth of the sample. On the other hand, in some cases, information on the properties of the material is obtained by generating carriers with a light of energy smaller than the band gap. The photon energy can be chosen fixed and monochromatic, as in the case of the below gap modulated photocurrent spectroscopy (BG-MPC) [6], or can be varied in a given range, as in the case of the constant photocurrent method (CPM) [7]. The different types of illuminations, wavelengths, and temporal/spatial shapes of the flux used for each characterization technique are detailed in Table 2.1, along with the name of each experiment.

To determine the opto-electronic parameters, linked to the density of states of the studied material, all the experiments are performed the sample being maintained in a steady state to which a perturbation is added. This perturbation can be a transient modification as in the case of the transient photocurrent experiment (TPC) [8, 9], in which a short (~ 3 ns) pulse of light is shone onto a sample maintained in the dark. This is also the case of the photoinduced transient spectroscopy (PITS), consisting in the analysis of the decrease of transient photocurrents after a light pulse has filled some trap states with electrons or holes [10]. The modification of the steady-state situation can also be a periodic variation of the flux in time, as for the modulated photocurrent experiments (MPC [11] and BG-MPC [6]), or a periodic variation of the flux in space, like in the steady state photocarrier grating (SSPG) technique [12, 13]. Besides, the modulations in time and space can be combined as, for example, in the case of the modulated photocarrier grating experiment (MPG) [14]. For some

experiments the perturbation comes from the modification of the light wavelength, as in the CPM, where the photon flux is adjusted after each change in wavelength in order to maintain the steady-state photocurrent constant during all the experiment. The case of the Fourier transform infrared spectroscopy (FTPS) [15, 16] is a little bit more tricky, since the contributions of the wavelengths are varied in the global flux of light by means of the moving mirror of a Michelson interferometer.

Table 2.1. Summary of some of the characterization techniques based on photoconductivity, indicating the type of illumination, the wavelength and the temporal shape of the flux for each of them. The photon energy of the light, $h\nu$, is compared to the bandgap width E_g. The experiments presented in this work are in bold characters.

Illumination	**Wavelength**	**Flux temporal shape**	**Experiments**
Uniform	Fixed, $h\nu > E_g$	Steady	Steady State Photocurrent (**SSPC**)
	Fixed, $h\nu > E_g$	Modulated	Modulated Photocurrent (**MPC**) at High (HF) and Low (LF) Frequency
	Fixed, $h\nu < E_g$	Modulated	Below Gap Modulated Photo-current (BG-MPC)
	Fixed, $h\nu > E_g$	Transient	Transient Photocurrent (TPC) Photoinduced Transient Spectroscopy (PITS)
Uniform	Changing, $h\nu$ swept from $h\nu < E_g$ to $h\nu > E_g$.	Steady but adjustable	Constant Photocurrent Method (**CPM**)
	Polychromatic, with $h\nu < E_g$ and $h\nu > E_g$.	Alternating from a Michelson interferometer	Fourier Transform Photocurrent Spectroscopy (**FTPS**)
Interferences	Fixed, $h\nu > E_g$	Steady	Steady State Photocarrier Grating (**SSPG**)
	Fixed, $h\nu > E_g$	Modulated	Modulated Photocarrier Grating (**MPG**)
	Fixed, $h\nu > E_g$	Moving (DC)	Moving Grating Technique (**MGT**)
	Fixed, $h\nu > E_g$	Moving (AC)	Oscillating Photocarrier Grating (**OPG**)

This chapter and the next two aim at presenting some of the characterization techniques based on the photoconductivity of the material under investigation. Chapter 2 will be dedicated to experiments in which the illumination of the sample is spatially uniform and monochromatic. In section 2.2 we shall present the simplest technique: the steady-state photoconductivity. In section 2.3 we shall describe the modulated photocurrent experiment. We shall deal only with experiments for which the photon energy is larger than the band gap. Although the BG-MPC has the advantage of being applicable directly to devices instead of coplanar samples, only very few groups have applied it to a rather limited range of materials [6, 17, 18]. For the same reasons we will not present the PITS and TPC experiments. Besides, it was shown that the MPC experiment is the Fourier transform of the TPC experiment (for a review of the advantages and drawbacks of each experiment, MPC and TPC, see for instance [9]).

In chapter 3 we shall present characterization techniques using the variations of the wavelength of the light source to probe the DOS of the material: CPM and FTPS. The theoretical and experimental

bases of these techniques will be described. It will be shown how they are complementary to the techniques based on a band to band generation with a uniform illumination. Applications to photovoltaic devices, as well as to new materials for solar conversion, such as perovskites, will be illustrated by experimental results.

In chapter 4 we shall describe the experiments for which the light is regularly distributed on the surface of the sample, starting with the basic principles of these techniques in section 4.1. In these experiments the inter-electrode gap is illuminated by interferences with different grating spacings. Under steady-state situation this gives rise to the SSPG technique, presented in section 4.2. By changing slightly the experimental conditions, and to introduce a temporal component in the SSPG technique, Hattori and coworkers have chosen to work with a spatially fixed grating which is modulated in time, giving rise to the MPG technique presented in section 4.3 [14]. Another way to introduce a temporal component in the SSPG technique is to move the grating at a constant speed in a direction perpendicular to the electrodes. This technique, the moving grating technique (MGT) presented in section 4.4, was proposed by U. Haken, M. Hundhausen and L. Ley [19, 20]. Finally, by changing slightly the experimental conditions, the steady movement of the grating can be modified into an oscillating movement between the electrodes, transforming the MGT into the oscillating photocarrier grating technique (OPG), presented in section 4.5 [21, 22]. Each method brings some new insights on the opto-electronic properties of the material, and we shall show in section 4.6 that from a characteristic time extracted from MGT and OPG a DOS spectroscopy can be achieved.

For all these techniques, we shall describe briefly how the experiment is performed. In order to link the measured quantities to the material transport parameters we shall first present the basic equations on which these techniques rely, underlying the range of validity of the experiment or some of their limitations. Then, we shall show how the DOS can be extracted from the experimental results, illustrating in some cases the potentiality of each technique by means of simulations. These simulations were developed at the Geeps as well as at the IFIS and the results were cross-checked to ensure their validity. One of these simulations is available at the Geeps website [23]. In addition, we shall underline that some techniques are 'connected', that is, how the basic results of one particular experiment can be linked to the results of another one, underlying their complementarities. Finally, for each technique, we shall present some experimental results on different types of materials, after a brief description of the experimental set-up fulfilling the requirements of the theoretical background.

2.2. Steady-state photoconductivity (SSPC)

The steady-state photoconductivity is one of the most performed experiments when dealing with photoconductive semiconductors, for it is easy to implement and brings an immediate knowledge of the photoconductive properties of the material. To achieve this simple experiment the sample is fitted with two parallel ohmic electrodes, biased with a DC voltage and illuminated with a given flux F_{dc} of monochromatic light that generates carriers from one band to the other. The photon energy must be chosen slightly larger than the bandgap energy to generate carriers as deep as possible in the material, limiting the influence of the top surface. From the excess of current compared to the dark situation one deduces the photoconductivity σ, which can be linked to some of the transport parameters of the material via

$$\sigma = q\left(\mu_n \Delta n + \mu_p \Delta p\right) \quad , \qquad (2.1)$$

where q is the absolute value of the electron charge, μ_n (μ_p) the extended states electron (hole) mobility and Δn (Δp) the excess of electron (hole) concentration compared to the dark situation. Defining the electron and hole lifetimes by

$$\tau_{\mathrm{n}} = \frac{\Delta n}{G_{\mathrm{dc}}} \quad , \qquad (2.2a)$$

$$\tau_{\mathrm{p}} = \frac{\Delta p}{G_{\mathrm{dc}}} \quad , \qquad (2.2b)$$

where G_{dc} is the band-to-band generation rate, the photoconductivity can be written in terms of the sum of the mobility × lifetime products as

$$\mu_{\mathrm{n}}\tau_{\mathrm{n}} + \mu_{\mathrm{p}}\tau_{\mathrm{p}} = \sigma/qG_{\mathrm{dc}} \quad . \qquad (2.3)$$

In many semiconductors (CdS, Sb_2S_3, hydrogenated amorphous silicon (a-Si:H), …) a power-law dependence between the photoconductivity and the generation rate has been observed in a given range of fluxes or temperatures: $\sigma \propto G_{\mathrm{dc}}^{\gamma}$, introducing the so-called γ factor or coefficient. Generally, one finds $\gamma < 1$. However, in some materials, and in particular in a-Si:H, a thermal quenching of the photoconductivity can be observed, *i.e.* a decrease of the photoconductivity with increasing temperature, accompanied by a superlinear generation dependence: $\gamma > 1$. This behavior was explained by A. Rose [4] as due to a change in the recombination channel from one defect state to another as the temperature is varied, a process that was called sensitization.

The work of A. Rose also underlined that a link exists between γ and the density of states (DOS) of the studied materials, and several authors have proposed models to connect γ to the DOS [24-27]. The power-law dependence of the photoconductivity upon generation rate is generally adjusted in a given range of generation rates. Changing this range also changes the value of γ, meaning that the power-law dependence has a local character. A more general definition of the γ factor can be proposed as

$$\gamma = \frac{\delta \ln(\sigma)}{\delta \ln(G_{\mathrm{dc}})} \quad . \qquad (2.4)$$

We shall show that an expression of γ related to the DOS can be deduced from analytical calculations, and thereby we shall propose a method to achieve a spectroscopy of the DOS of the material.

2.2.1 Basic equations

We consider an undoped semiconductor containing m species of monovalent states (for defects having two charged states, either neutral or charged) within the gap. The species of states were defined by Simmons and Taylor [28] according to their respective capture coefficients for electrons ($C_{\mathrm{n}}^{\mathrm{i}}$) and holes ($C_{\mathrm{p}}^{\mathrm{i}}$), with $1 \le i \le m$; belonging to the same species all the states having the same value for the ratio $C_{\mathrm{n}}^{\mathrm{i}}/C_{\mathrm{p}}^{\mathrm{i}}$. For this semiconductor, enlightened by a uniformly absorbed DC light flux creating free carriers by band-to-band generation, the continuity and charge neutrality equations are

$$\frac{\partial n}{\partial t} = G_{\mathrm{dc}} - \sum_1^m \int_{E_{\mathrm{V}}}^{E_{\mathrm{C}}} \{\bar{n}^{\mathrm{i}}[1 - f^{\mathrm{i}}] - e_{\mathrm{n}}^{\mathrm{i}} f^{\mathrm{i}}\} N^{\mathrm{i}} dE + \frac{1}{q}\mathrm{div}(\vec{J}_{\mathrm{n}}) \quad , \qquad (2.5)$$

$$\frac{\partial p}{\partial t} = G_{\mathrm{dc}} - \sum_1^m \int_{E_{\mathrm{V}}}^{E_{\mathrm{C}}} \{\bar{p}^{\mathrm{i}} f^{\mathrm{i}} - e_{\mathrm{p}}^{\mathrm{i}}[1 - f^{\mathrm{i}}]\} N^{\mathrm{i}} dE - \frac{1}{q}\mathrm{div}(\vec{J}_{\mathrm{p}}) \quad , \qquad (2.6)$$

$$\varepsilon\varepsilon_0 \mathrm{div}(\vec{\xi}) = q\left\{p - p_0 - (n - n_0) - \sum_1^m \int_{E_{\mathrm{V}}}^{E_{\mathrm{C}}} N^{\mathrm{i}}(f^{\mathrm{i}} - f_0) dE\right\} \quad . \qquad (2.7)$$

In these equations, E_{V} (E_{C}) is the energy of the top (bottom) of the valence (conduction) band, n (p) is the density of electrons (holes) in the extended states (n_0 and p_0 being the values under dark equilibrium conditions), $\bar{n}^{\mathrm{i}} = nC_{\mathrm{n}}^{\mathrm{i}}$ ($\bar{p}^{\mathrm{i}} = pC_{\mathrm{p}}^{\mathrm{i}}$) is the capture rate of electrons (holes) from the i^{th} species of trap,

$e_{\mathrm{n}}^{\mathrm{i}}(E)$ ($e_{\mathrm{p}}^{\mathrm{i}}(E)$) is the energy-dependent emission rate of electrons (holes) from the i^{th} species of trap, $\vec{\boldsymbol{J}}_{\mathrm{n}}$ ($\vec{\boldsymbol{J}}_{\mathrm{p}}$) is the current density of electrons (holes), ε is the dielectric constant of the material, ε_0 is the vacuum permittivity, $\vec{\boldsymbol{\xi}}$ is the electric field between the electrodes, $N^{\mathrm{i}}(E)$ is the density of states of species i, $f^{\mathrm{i}}(E)$ is the occupation function of the i^{th} species of trap under illumination, and $f_0(E)$ is the occupation function under dark equilibrium conditions, which is assumed the same for all the traps and equal to the Fermi-Dirac distribution (degeneracy factors are neglected or can be taken into account in a modified energy position). In our analysis we consider only band-to-band generation, neglecting optical transitions involving localized states due to their much lower probability.

Some quantities in Eqs. (2.5)-(2.7) are energy dependent and some are not. The densities of states $N^{\mathrm{i}}(E)$, the occupation functions $f^{\mathrm{i}}(E)$ and the emission rates of electrons and holes $e_{\mathrm{n}}^{\mathrm{i}}(E)$ and $e_{\mathrm{p}}^{\mathrm{i}}(E)$ are all energy dependent quantities, but to lighten the equations we shall omit the formal (E) for all of them in the following. We have assumed that the capture coefficients, $C_{\mathrm{n}}^{\mathrm{i}}$ and $C_{\mathrm{p}}^{\mathrm{i}}$, do not depend on energy. The relation between the emission rates and the capture coefficients is given by a detailed balance study of the exchange of carriers, under thermal equilibrium conditions, between the extended states and a trapping level at energy E, leading to:

$$e_{\mathrm{n}}^{\mathrm{i}} = C_{\mathrm{n}}^{\mathrm{i}} N_{\mathrm{C}} \exp\left(-\frac{E_{\mathrm{C}}-E}{k_{\mathrm{B}}T}\right) \quad , \qquad (2.8)$$

and

$$e_{\mathrm{p}}^{\mathrm{i}} = C_{\mathrm{p}}^{\mathrm{i}} N_{\mathrm{V}} \exp\left(-\frac{E-E_{\mathrm{V}}}{k_{\mathrm{B}}T}\right) \quad , \qquad (2.9)$$

k_{B} being the Boltzmann's constant, T the absolute temperature, and N_{C} (N_{V}) the equivalent density of states at the bottom (top) of the conduction (valence) band. We make the usual assumption that the emission rates remain unaltered with respect to equilibrium conditions.

As a matter of simplification, considering uniform and steady-state illumination and ohmic contacts, we can assume that $\frac{\partial n}{\partial t} = 0$, $\frac{\partial p}{\partial t} = 0$, $\mathrm{div}(\vec{\boldsymbol{J}}_{\mathrm{n}}) = 0$, $\mathrm{div}(\vec{\boldsymbol{J}}_{\mathrm{p}}) = 0$, and $\mathrm{div}(\vec{\boldsymbol{\xi}}) = 0$. The expression for f^{i} is

$$f^{\mathrm{i}} = \left(\bar{n}^{\mathrm{i}} + e_{\mathrm{p}}^{\mathrm{i}}\right)\tau^{\mathrm{i}} \quad , \qquad (2.10)$$

with

$$\tau^{\mathrm{i}} = \frac{1}{\bar{n}^{\mathrm{i}}+\bar{p}^{\mathrm{i}}+e_{\mathrm{p}}^{\mathrm{i}}+e_{\mathrm{n}}^{\mathrm{i}}} \quad . \qquad (2.11)$$

From the continuity equations, Eqs. (2.5)-(2.6), the electron (hole) lifetime τ_{n} (τ_{p}) can be defined. Indeed, a very simple calculation leads to

$$G_{\mathrm{dc}} = \sum_1^m G_{\mathrm{dc}}^{\mathrm{i}} = \sum_1^m \int_{E_{\mathrm{V}}}^{E_{\mathrm{C}}} \left(\bar{n}^{\mathrm{i}}\bar{p}^{\mathrm{i}} - e_{\mathrm{n}}^{\mathrm{i}}e_{\mathrm{p}}^{\mathrm{i}}\right)\tau^{\mathrm{i}}N^{\mathrm{i}}dE \quad , \qquad (2.12)$$

where the product $e_{\mathrm{n}}^{\mathrm{i}}e_{\mathrm{p}}^{\mathrm{i}}$ can be neglected [29]. Thus, using Eqs. (2.2a) and (2.2b), one ends with

$$\frac{1}{\tau_{\mathrm{n}}} = \sum_1^m \frac{1}{\tau_{\mathrm{n}}^{\mathrm{i}}} = \sum_1^m C_{\mathrm{n}}^{\mathrm{i}}\bar{p}^{\mathrm{i}} \int_{E_{\mathrm{V}}}^{E_{\mathrm{C}}} \tau^{\mathrm{i}}N^{\mathrm{i}}dE \quad , \qquad (2.13)$$

and

$$\frac{1}{\tau_{\mathrm{p}}} = \sum_1^m \frac{1}{\tau_{\mathrm{p}}^{\mathrm{i}}} = \sum_1^m C_{\mathrm{p}}^{\mathrm{i}}\bar{n}^{\mathrm{i}} \int_{E_{\mathrm{V}}}^{E_{\mathrm{C}}} \tau^{\mathrm{i}}N^{\mathrm{i}}dE \quad . \qquad (2.14)$$

If one changes slightly the photon flux, several quantities Q (*e.g.* G_{dc}, f^i, $\bar{n}^i$, $\bar{p}^i$, n and p) appearing in Eqs. (2.5)-(2.7) will exhibit a change δQ. By differentiation, one can deduce the expression of δf^i

$$\delta f^i = f^i\left(1-f^i\right)\left[\frac{\delta\bar{n}^i}{\bar{n}^i+e_p^i}-\frac{\delta\bar{p}^i}{\bar{p}^i+e_n^i}\right] \quad . \qquad (2.15)$$

Introducing Eq. (2.15) in the continuity equations gives

$$\delta G_{dc} = \delta n\sum_1^m C_n^i\int_{E_V}^{E_C}\left(1-f^i\right)\left(\bar{p}^i+e_p^i\right)\tau^i N^i dE + \delta p\sum_1^m C_p^i\int_{E_V}^{E_C} f^i\left(\bar{n}^i+e_n^i\right)\tau^i N^i dE, \qquad (2.16)$$

and for the charge neutrality equation

$$\delta n\left(1+\sum_1^m C_n^i\int_{E_V}^{E_C}\left(1-f^i\right)\tau^i N^i dE\right) = \delta p\left(1+\sum_1^m C_p^i\int_{E_V}^{E_C} f^i\tau^i N^i dE\right) \quad . \qquad (2.17)$$

Combining Eq. (2.17) with Eq. (2.16) gives

$$\delta G_{dc} = \frac{\delta p}{\tau_p'} = \frac{\delta n}{\tau_n'} \quad , \qquad (2.18)$$

where

$$\frac{1}{\tau_n'} = \sum_1^m C_n^i\int_{E_V}^{E_C}\left(1-f^i\right)\left(\bar{p}^i+e_p^i\right)\tau^i N^i dE + \sum_1^m C_p^i\int_{E_V}^{E_C} f^i\left(\bar{n}^i+e_n^i\right)\tau^i N^i dE\,\frac{1+\sum_1^m C_n^i\int_{E_V}^{E_C}\left(1-f^i\right)\tau^i N^i dE}{1+\sum_1^m C_p^i\int_{E_V}^{E_C} f^i\tau^i N^i dE} \quad , \qquad (2.19)$$

and

$$\frac{1}{\tau_p'} = \sum_1^m C_p^i\int_{E_V}^{E_C} f^i\left(\bar{n}^i+e_n^i\right)\tau^i N^i dE + \sum_1^m C_n^i\int_{E_V}^{E_C}\left(1-f^i\right)\left(\bar{p}^i+e_p^i\right)\tau^i N^i dE\,\frac{1+\sum_1^m C_p^i\int_{E_V}^{E_C} f^i\tau^i N^i dE}{1+\sum_1^m C_n^i\int_{E_V}^{E_C}\left(1-f^i\right)\tau^i N^i dE} \quad . \qquad (2.20)$$

These two quantities, τ_n' and τ_p', can be considered as the lifetime of the excess carriers created by the excess generation rate δG_{dc}, and they are different from τ_n and τ_p defined in Eqs. (2.13)-(2.14).

The γ factor introduced by Eq. (2.4) can thus be written in terms of the various lifetimes:

$$\gamma = \frac{\mu_n\tau_n'+\mu_p\tau_p'}{\mu_n\tau_n+\mu_p\tau_p} \quad , \qquad (2.21)$$

which, from the above equations, can be written as a function of the DOS:

$$\gamma = \frac{\frac{1}{\left(\mu_n\tau_n+\mu_p\tau_p\right)}\left[\mu_n\left(1+\sum C_p^i\int f^i\tau^i N^i dE\right)+\mu_p\left(1+\sum C_n^i\int\left(1-f^i\right)\tau^i N^i dE\right)\right]}{\sum C_n^i\int\left(1-f^i\right)\left(\bar{p}^i+e_p^i\right)\tau^i N^i dE\left(1+\sum C_p^i\int f^i\tau^i N^i dE\right)+\sum C_p^i\int f^i\left(\bar{n}^i+e_n^i\right)\tau^i N^i dE\left(1+\sum C_n^i\int\left(1-f^i\right)\tau^i N^i dE\right)} \quad , \qquad (2.22)$$

where the sums (Σ) are over the *m* species of states and the integrals are between E_V and E_C.

2.2.2 DOS determination

Equation (2.22) can be shortened applying some simplifying assumptions. Firstly, **if trapped carriers are much more numerous than free carriers** (as usual in highly defective semiconductors such as a-Si:H), the "1" in the parenthesis $\left(1+\sum C_{\mathrm{p}}^{\mathrm{i}}\int f^{\mathrm{i}}\tau^{\mathrm{i}}N^{\mathrm{i}}dE\right)$ and $(1+\sum C_{\mathrm{n}}^{\mathrm{i}}\int(1-f^{\mathrm{i}})\tau^{\mathrm{i}}N^{\mathrm{i}}dE)$ can be neglected. Secondly, **if electrons are the majority carriers and are more mobile than holes** (as is the case for undoped a-Si:H), then $\mu_{\mathrm{n}}\tau_{\mathrm{n}} >> \mu_{\mathrm{p}}\tau_{\mathrm{p}}$. Thirdly, **if the energy dependence of the DOS is not stronger than that of the Boltzmann distribution** $e^{E/k_{\mathrm{B}}T}$, the integrals of Eq. (2.22) can be approximated as shown by Schmidt and co-workers [30]. Under these assumptions, Eq. (2.22) transforms into

$$\frac{1}{\gamma}-1=\frac{\sum_1^m N_{\mathrm{n}}^{\mathrm{i}}}{\sum_1^m G_{\mathrm{dc}}^{\mathrm{i}}\tau_{\mathrm{t}}^{\mathrm{i}}}=\frac{\sum_1^m N_{\mathrm{n}}^{\mathrm{i}}}{\sum_1^m \frac{1}{C_{\mathrm{n}}^{\mathrm{i}}\tau_{\mathrm{n}}^{\mathrm{i}}}} \quad . \qquad (2.23)$$

In this equation $\tau_{\mathrm{n}}^{\mathrm{i}}$ is defined by Eq. (2.13) and $\tau_{\mathrm{t}}^{\mathrm{i}}$ is determined by the sum of the capture rates of electrons and holes as

$$\tau_{\mathrm{t}}^{\mathrm{i}}=\frac{1}{C_{\mathrm{n}}^{\mathrm{i}}n+C_{\mathrm{p}}^{\mathrm{i}}p} \quad , \qquad (2.24)$$

$N_{\mathrm{n}}^{\mathrm{i}}=k_{\mathrm{B}}TN\left(E_{\mathrm{tn}}^{\mathrm{i}}\right)$, $N(E_{\mathrm{tn}}^{\mathrm{i}})$ being the density of states at the quasi Fermi level $E_{\mathrm{tn}}^{\mathrm{i}}$ for electrons trapped in the i^{th} species of states defined by

$$e_{\mathrm{n}}\left(E_{\mathrm{tn}}^{\mathrm{i}}\right)=\frac{1}{\tau_{\mathrm{t}}^{\mathrm{i}}} \quad . \qquad (2.25)$$

If there is a single species of states in the gap, or if one species of state dominates the recombination, Eq. (2.23) further simplifies into $\frac{1}{\gamma}-1=C_{\mathrm{n}}\tau_{\mathrm{n}}N_{\mathrm{n}}$, from which a simple expression for the DOS at the quasi Fermi level of trapped electrons can be obtained:

$$\frac{N(E_{\mathrm{tn}})C_{\mathrm{n}}}{\mu_{\mathrm{n}}}=\frac{G_{\mathrm{dc}}}{k_{\mathrm{B}}T\mu_{\mathrm{n}}n}\left[\frac{1}{\gamma}-1\right]=\frac{qG_{\mathrm{dc}}}{k_{\mathrm{B}}T\sigma}\left[\frac{1}{\gamma}-1\right] \quad . \qquad (2.26)$$

Since the electrons are the majority carriers, the quasi Fermi level for trapped electrons, E_{tn}, almost coincides with the quasi Fermi level for free electrons E_{Fn}, $E_{\mathrm{tn}} \approx E_{\mathrm{Fn}}$, which can be obtained from the photoconductivity σ as

$$E_{\mathrm{C}}-E_{\mathrm{Fn}}=k_{\mathrm{B}}T\ln\left[\frac{q\mu_{\mathrm{n}}N_{\mathrm{C}}}{\sigma}\right] \quad . \qquad (2.27)$$

Equations (2.26) and (2.27) allow one to perform a DOS spectroscopy, *e.g.* the reconstruction of the density of states interacting with free electrons, using the evolution of γ with flux and/or with temperature. Of course, a supralinear dependence of the photoconductivity on the generation rate ($\gamma > 1$), such as the one observed in some a-Si:H samples at low temperatures, would cause Eq. (2.26) to give unreasonable negative values. This sensitization effect appears when different species of traps are present such that the approximations to transform Eq. (2.22) into Eq. (2.23) are no longer valid.

The case where two different species of states are present in the gap, leading to a sensitization effect, is rather difficult to visualize directly from equations. That is why we have developed a numerical calculation to shine light on the consequences of the presence of two different species of states on the DOS determination.

2.2.3 Illustration by means of simulations

To illustrate the possibility of a DOS spectroscopy from the determination of γ and its evolution with temperature, we have performed some numerical calculations starting from transport parameters and density of states typical of a-Si:H. We shall not recall all the details of the transport parameters and DOS we have chosen. For these details one can refer to [31].

The band gap was taken equal to 1.8 eV and a 'standard' DOS was defined, made of the sum of two exponential band tails and deep defect distributions. The exponential conduction band tail (CBT) is varying as $\exp\left[\frac{E-E_C}{k_B T_C}\right]$ while the valence band tail (VBT) is varying as $\exp\left[\frac{E_V-E}{k_B T_V}\right]$, and we have chosen the default values of the characteristic temperatures to be T_C = 275 K and T_V = 600 K, in agreement with reports of the literature for device grade films [32, 33]. The densities of states at the band edges were taken equal to $N(E_C) = N(E_V) = 10^{21}$ cm^{-3}eV^{-1} leading to equivalent densities of states of the order of those of crystalline silicon $N_C = N_V = 2.5\times10^{19}$ cm^{-3} [34]. The deep states were modeled by Gaussian distributions of acceptor and donor states located at 0.35 eV and 1.1 eV below the conduction band edge, with standard deviations of 0.15 eV and 0.2 eV, respectively, and with the same maximum value of 3×10^{16} cm^{-3}eV^{-1}. With this overall distribution of states, the location of the dark Fermi level, E_{F0}, is $E_C - E_{F0}$ = 0.67 eV. The density of states $N(E)$ resulting from this parameter choice is presented in Fig. 2.1.

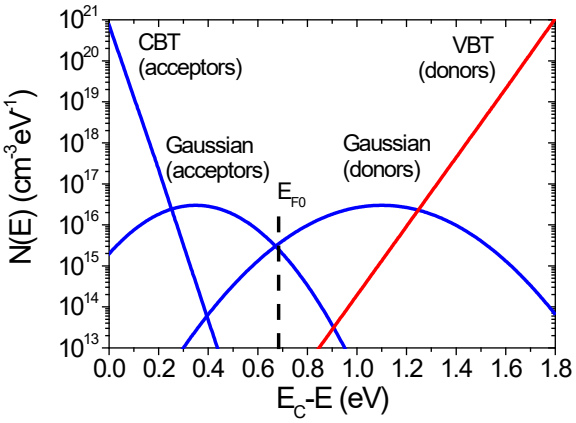

Figure 2.1. Density of band gap states introduced in our calculation, typical of device grade a-Si:H (for details see text). The position of the dark Fermi level E_{F0} is indicated by the vertical dashed line.

The most important parameters to be considered to define the species of states are the capture coefficients. To introduce different types of states we have assumed that for type *I*, concerning only the valence band tail states (red line in Fig. 2.1), the capture coefficients for electrons and holes were respectively $C_n^I = 2\times10^{-9}$ cm^{3}s^{-1} and $C_p^I = 10^{-8}$ cm^{3}s^{-1}. For the second type of states (blue lines in Fig. 2.1), including the CBT, the acceptor and the donor deep states, the capture coefficients for electrons and holes were respectively $C_n^{II} = 2\times10^{-8}$ cm^{3}s^{-1} and $C_p^{II} = 10^{-8}$ cm^{3}s^{-1}. With this choice we have a ratio $C_n^{II}/C_n^I = 10$ (while $C_p^{II}/C_p^I = 1$).

Figure 2.2 presents the results of calculations performed with the above parameters and for several values of T_V. The temperature of the 'sample' was varied from 90 K to 450 K in 10-K steps and the flux was fixed at $F_{dc} = 5\times10^{14}$ cm^{-2}s^{-1}. Actually, since from Eq. (2.26) we cannot obtain the DOS but only the quantity NC/μ, in this figure we compare the NC/μ values reconstructed from the calculation of γ and σ at different temperatures (γ-NC/μ, symbols) to the ones introduced in the calculation (lines).

As can be seen in this figure, with a characteristic temperature T_V = 600 K there is no agreement between the reconstructed γ-NC/μ (red squares) and the introduced NC/μ (black full lines).

At high and low energies the γ-NC/μ is well below the true NC/μ, and there is even an energy range (0.35 – 0.5 eV) where the γ-NC/μ could not be calculated for in this region we find $\gamma > 1$. This behavior corresponds to the sensitization phenomenon and, indeed, in the temperature region where $\gamma > 1$ the photoconductivity exhibits a clear thermal quenching as shown in Fig. 2.3.

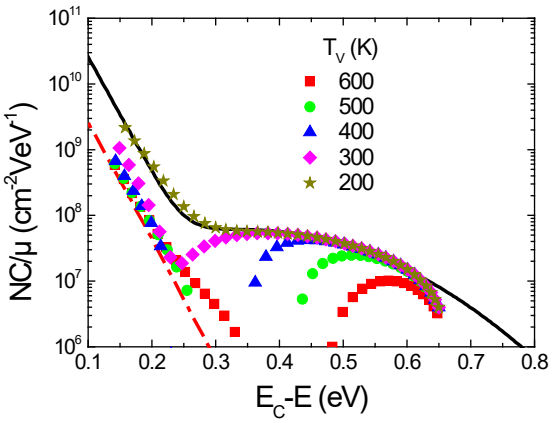

Figure 2.2. Reconstructions of several γ-NC/μ curves (symbols) deduced from Eq. (2.26) after calculation of γ at different temperatures, for different values of the characteristic temperature of the VBT indicated in the inset. These reconstructions are compared to the actual NC/μ introduced in the calculation (black full line).

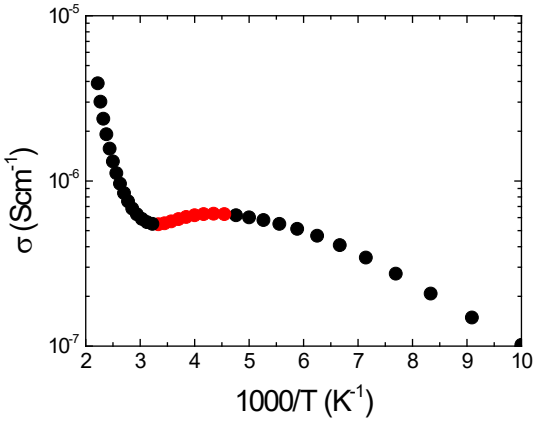

Figure 2.3. Arrhenius plot of the photo-conductivity with a 'material' presenting a characteristic temperature of the VBT $T_V = 600$ K. The photoconductivity quenching is indicated in red dots in the figure

In the present case, this sensitization effect can be explained in the following way. According to Taylor and Simmons [29], for a given type of states the recombination zone in a semiconductor corresponds to the energy range in between the quasi Fermi levels for trapped electrons, E_{tn}, and for trapped holes, E_{tp}. Since $e_n(E)$ and $e_p(E)$ depend exponentially on $1/T$, at a given generation rate and at low temperature, the splitting of the quasi Fermi levels is wide and a large number of states are contained in the recombination zone, including those of the VBT which have a lower electron capture coefficient than the other states. Actually, the simulation shows that due to the large splitting of the quasi Fermi levels, the deep defect contribution to the recombination is much less than the contributions of the CBT and VBT states. With increasing temperature, the photoconductivity increases steadily but the width of the recombination zone decreases, and so does the number of VBT states included in this zone, because of the exponential decrease of the VBT DOS. If the main recombination path shifts from the VBT states to the other states, the recombination rate is suddenly enhanced because $C_n^{II} = 10 \times C_n^{I}$ and, at first, this results in a decrease of the photoconductivity with increasing temperature. Subsequently, with a still increasing temperature, σ resumes its increase as expected in a material where no sensitization is observed.

To minimize the influence of the VBT, its characteristic temperature T_V was decreased to 200 K in 100 K steps. It can be seen in Fig. 2.2 that the influence of the sensitization effect clearly decreases with decreasing T_V, according to the shrinking of the energy range where we found $\gamma > 1$, to

eventually end with an excellent match between the γ-NC/μ (yellow stars) and the introduced NC/μ. This is the result predicted by Eqs. (2.26)-(2.27), applicable when one deals with a single species of states.

The last point to explain is the fact that at low temperatures, when the recombination path is dominated by the VBT states, for T_V = 300, 400, 500 and 600K the γ-NC/μ is systematically 10 times lower than the 'true' NC/μ at low energies though it follows the same exponential decrease as the CBT (dashed-dotted red line in Fig. 2.2). If we neglect the holes contribution, from Eq. (2.23) we have

$$\frac{1}{\gamma} - 1 = \frac{C_n^I N_n^{II}}{\frac{1}{\tau_n^I} + \frac{1}{10\tau_n^{II}}} \quad , \qquad (2.28)$$

in which N_n^I has been omitted since it corresponds to the density of the exponentially decreasing VBT taken at E_{tn}. In addition, due to the peculiar shape of the DOS, having a large VBT and a narrow CBT, the total number of states between the quasi Fermi levels is dominated by those of the VBT. This means that the dominating term at the denominator of Eq. (2.28) is $1/\tau_n^I = 1/\tau_n$ that leads to

$$\frac{1}{\gamma} - 1 = C_n^I \tau_n N_n^{II} \quad . \qquad (2.29)$$

Thus, the γ-NC/μ values take into account the coefficient C_n^I of the VBT, ten times lower than that of the CBT, which results into a reconstructed distribution of states roughly ten times lower than the actual one, as observed in Fig. 2.2 (dashed-dotted red line).

The same type of numerical calculation was performed with a 'crystalline' material having different species of states, and the same behavior was found: the capture coefficient to take into account in Eq. (2.28) is that of the states that dominate the recombination [31]. This property will be very useful to experimentally extract some transport parameters of the material, particularly when the γ-NC/μ spectroscopy is used with other characterization techniques, as the modulated photocurrent experiment.

2.3. Modulated photocurrent (MPC)

The modulated photocurrent (MPC) experiment was proposed in 1981 by H. Oheda [11] as a characterization technique to achieve a spectroscopy of the density of states in the bandgap of semiconductors. The basic idea of this technique is to illuminate the gap in between the electrodes of a coplanar sample by a steady flux of a monochromatic light, with a photon energy larger than the band gap, that fixes the steady state of the sample. To this DC flux is superimposed a small AC perturbation, made of an alternating flux of the same wavelength at an angular frequency ω. Assuming that one type of carrier is predominant, the multiple trapping exchanges of these carriers between extended and trap states lead to a phase shift between the AC flux and the generated AC current. Oheda has shown that, by recording at different ω the phase shift of the AC current referred to that of the AC flux, it was possible, with a recursive method, to achieve a spectroscopy of the density of localized states present in the gap and exchanging carriers with the extended states. This technique was largely improved by R. Brüggemann and co-workers [35] taking into account both the modulus and the phase shift of the AC photocurrent, a method which lightens and simplifies Oheda's recursive method.

However, in both methods the authors have assumed that the transport was unipolar, i.e., dominated by one type of carrier. This is far to be the case for all the materials, especially when they are studied in coplanar geometry where electrons and holes can both play an important role in the transport mechanisms. That is why a complete analysis of the MPC technique has been developed to understand the contribution of each type of carrier to the alternating current generated by the

alternating flux of the MPC technique [36], [37]. After a brief presentation of the experimental bench used to perform the MPC characterizations, we shall present the theoretical backgrounds of this experiment.

In Fig. 2.4 we present the schematic diagram of an MPC bench. The sample is fixed on the cold finger of a cryostat and illuminated by the light coming from a group of light emitting diodes (LEDs). The advantage of LEDs is that it is easy to obtain the superimposition of a quasi-monochromatic DC light and an alternating component on a large range of frequencies, say from 1 Hz to 100 kHz. A voltage bias is applied to the sample and the resulting current is amplified and transformed into a voltage signal by a current-voltage amplifier. The AC part is then recorded and analyzed in terms of modulus and phase shift by a lock-in amplifier, using the modulation voltage signal of the LEDs as a reference. The experiment can be fully computer-controlled, which makes it very easy to use. Neutral density filters (ND) can be inserted between the LEDs and the film to attenuate the flux of light if necessary. These filters are of primary importance to fix the regime under which the MPC experiment is performed. Indeed, for reasons that will appear clearly in the following, the MPC experiment can be applied in two regimes: the high frequency regime, obtained with a low flux of DC light, and the low frequency regime, obtained with a high flux of DC light. The last point to underline is the fact that the whole measurement chain presents a transfer function that may distort the phase shift and/or the modulus of the measured AC signal. That is why, prior to any measurements, a calibration must be done with a fast photodiode in place of the sample, to subsequently subtract the phase shift linked to the measurement chain and correct the signal.

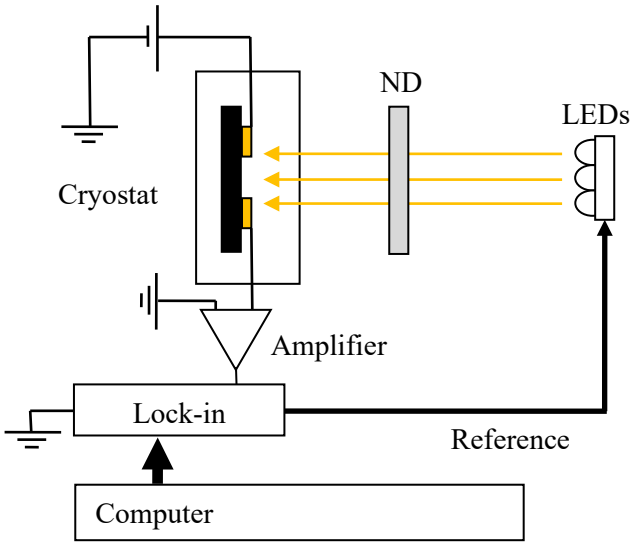

Fig. 2.4. Schematic diagram of an MPC bench.

To simplify the theoretical developments, we shall consider in the following a DOS made of a single species of monovalent states. The following calculations can be easily extended to the case where several types of defect states are present in the gap. We assume here that the generation rate is homogeneous in a volume $S \times d$, d being the inter-electrode distance and S the section where the photocurrent flows with a homogeneous photocurrent density. Assuming a homogeneous electric field in between the electrodes, we start from the same continuity equations as in the case of SSPC (see Eqs. (2.5) and (2.6)), in which the divergences of the currents are equal to 0,

$$\frac{\partial n}{\partial t} = G - \int_{E_V}^{E_C} \{\bar{n}[1 - f(E)] - e_n(E) f(E)\} N(E) dE \quad , \qquad (2.30)$$

$$\frac{\partial p}{\partial t} = G - \int_{E_V}^{E_C} \{\bar{p} f(E) - e_p(E)[1 - f(E)]\} N(E) dE \quad . \qquad (2.31)$$

To these equations we have to add an equation linking the occupation function $f(E)$ to the other quantities. From the Shockley-Read-Hall statistics [38 - 40] we have

$$\frac{\partial f(E)}{\partial t} = \bar{n} + e_{\mathrm{p}}(E) - f(E)\left[\bar{n} + \bar{p} + e_{\mathrm{n}}(E) + e_{\mathrm{p}}(E)\right] \quad . \tag{2.32}$$

Since the illumination of the film is made of a steady flux plus an alternating one, all the quantities in Eqs. (2.30)-(2.32), except the emission rates and the density of states, can be decomposed into a steady-state component indexed "dc" and an alternating component indexed "ac″. For instance, n can be replaced by $n = n_{\mathrm{dc}} + n_{\mathrm{ac}}\exp(j\omega t)$, where t is the time and j the square root of -1. If we consider the alternating component, Eqs. (2.30) and (2.31) lead to

$$j\omega n_{\mathrm{ac}} = G_{\mathrm{ac}} + \int_{E_{\mathrm{V}}}^{E_{\mathrm{C}}} \{[\bar{n}_{\mathrm{dc}} + e_{\mathrm{n}}(E)]f_{\mathrm{ac}}(E) - \bar{n}_{\mathrm{ac}}[1 - f_{\mathrm{dc}}(E)]\}\, N(E)dE \quad , \tag{2.33}$$

$$j\omega p_{\mathrm{ac}} = G_{\mathrm{ac}} - \int_{E_{\mathrm{V}}}^{E_{\mathrm{C}}} \left\{\left[\bar{p}_{\mathrm{dc}} + e_{\mathrm{p}}(E)\right]f_{\mathrm{ac}}(E) + \bar{p}_{\mathrm{ac}} f_{\mathrm{dc}}(E)\right\} N(E)dE \quad , \tag{2.34}$$

and Eq. (2.32) gives

$$f_{\mathrm{ac}}(E) = \frac{\bar{n}_{\mathrm{ac}}[1 - f_{\mathrm{dc}}(E)] - \bar{p}_{\mathrm{ac}} f_{\mathrm{dc}}(E)}{j\omega + \frac{1}{\tau(E)}} \quad , \tag{2.35}$$

where

$$\frac{1}{\tau(E)} = \bar{n}_{\mathrm{dc}} + \bar{p}_{\mathrm{dc}} + e_{\mathrm{n}}(E) + e_{\mathrm{p}}(E) \quad . \tag{2.36}$$

If the expression of $f_{\mathrm{ac}}(E)$ is replaced into Eqs. (2.33) and (2.34), and if we write $n_{\mathrm{ac}} = n_{\mathrm{r}} + j\, n_{\mathrm{i}}$, $p_{\mathrm{ac}} = p_{\mathrm{r}} + j\, p_{\mathrm{i}}$, where the indices r and i stand for the real and imaginary parts, respectively, we can form a linear system of four equations [36]

$$\begin{pmatrix} A_{\mathrm{n}} & A_{\mathrm{p}} & B_{\mathrm{n}} & -B_{\mathrm{p}} \\ -B_{\mathrm{n}} & B_{\mathrm{p}} & A_{\mathrm{n}} & A_{\mathrm{p}} \\ A_{\mathrm{n}}^{*} & A_{\mathrm{p}}^{*} & -B_{\mathrm{n}}^{*} & B_{\mathrm{p}}^{*} \\ B_{\mathrm{n}}^{*} & -B_{\mathrm{p}}^{*} & A_{\mathrm{n}}^{*} & A_{\mathrm{p}}^{*} \end{pmatrix} \begin{pmatrix} n_{\mathrm{i}} \\ p_{\mathrm{i}} \\ n_{\mathrm{r}} \\ p_{\mathrm{r}} \end{pmatrix} = \begin{pmatrix} 0 \\ G_{\mathrm{ac}} \\ 0 \\ G_{\mathrm{ac}} \end{pmatrix} \quad , \tag{2.37}$$

with A_{n}, A_{p}, B_{n} and B_{p} given by

$$A_{\mathrm{n}} = C_{\mathrm{n}} \int_{E_{\mathrm{V}}}^{E_{\mathrm{C}}} \left[1 - \tau(E)\frac{\bar{n}_{\mathrm{dc}} + e_{\mathrm{n}}(E)}{1 + \omega^2\tau^2(E)}\right]\left(1 - f_{\mathrm{dc}}(E)\right)N(E)dE \quad , \tag{2.38}$$

$$A_{\mathrm{p}} = C_{\mathrm{p}} \int_{E_{\mathrm{V}}}^{E_{\mathrm{C}}} \tau(E)\frac{\bar{n}_{\mathrm{dc}} + e_{\mathrm{n}}(E)}{1 + \omega^2\tau^2(E)} f_{\mathrm{dc}}(E)N(E)dE \quad , \tag{2.39}$$

$$B_{\mathrm{n}} = C_{\mathrm{n}}\omega \int_{E_{\mathrm{V}}}^{E_{\mathrm{C}}} \tau^2(E)\frac{\bar{n}_{\mathrm{dc}} + e_{\mathrm{n}}(E)}{1 + \omega^2\tau^2(E)}\left(1 - f_{\mathrm{dc}}(E)\right)N(E)dE + \omega \quad , \tag{2.40}$$

$$B_{\mathrm{p}} = C_{\mathrm{p}}\omega \int_{E_{\mathrm{V}}}^{E_{\mathrm{C}}} \tau^2(E)\frac{\bar{n}_{\mathrm{dc}} + e_{\mathrm{n}}(E)}{1 + \omega^2\tau^2(E)} f_{\mathrm{dc}}(E)N(E)dE \quad , \tag{2.41}$$

and A_{n}^{*}, A_{p}^{*}, B_{n}^{*}, and B_{p}^{*} being obtained by a transformation of A_{p}, A_{n}, B_{p}, and B_{n}, respectively, using an operator $\mathcal{F}$ transforming all indexes ‘n’ into ‘p’, f into $(1 - f)$, and reciprocally. Note that with this transformation ω, $\tau(E)$ and $N(E)$ are unchanged. For instance one obtains

$$A_{\mathrm{n}}^{*} = \mathcal{F}\left(A_{\mathrm{p}}\right) = C_{\mathrm{n}} \int_{E_{\mathrm{V}}}^{E_{\mathrm{C}}} \left[\tau(E)\frac{\bar{p}_{\mathrm{dc}} + e_{\mathrm{p}}(E)}{1 + \omega^2\tau^2(E)}\right]\left(1 - f_{\mathrm{dc}}(E)\right)N(E)dE \quad . \tag{2.42}$$

Solving the system (2.37) for n_r, p_r, n_i and p_i, the alternating contribution, I_{ac}, to the photocurrent can be calculated from

$$I_{ac} = Sq\xi\,[\mu_n n_r + \mu_p p_r + j\,(\mu_n n_i + \mu_p p_i)] \quad . \qquad (2.43)$$

The phase shift ϕ and modulus of the photocurrent, such as $I_{ac} = \left| I_{ac} \right| \exp(-j\phi)$, are given by

$$\tan(\phi) = -\frac{\mu_n n_i + \mu_p p_i}{\mu_n n_r + \mu_p p_r} \quad , \qquad (2.44)$$

$$|I_{ac}| = Sq\xi\left[\left(\mu_n n_i + \mu_p p_i\right)^2 + \left(\mu_n n_r + \mu_p p_r\right)^2\right]^{1/2} \quad . \qquad (2.45)$$

Considering the physics involved, one can easily understand that two energy levels, $E_{\omega n}$ and $E_{\omega p}$, defined by

$$e_n(E_{\omega n}) = e_p(E_{\omega p}) = \omega \quad , \qquad (2.46)$$

play an important role. Indeed, depending on the relative position of these levels compared with the quasi Fermi levels for trapped carriers, E_{tn} and E_{tp}, (see Sec. 2.2.2 and Ref. [29]), two extreme cases can be considered:

- case (i), $\omega >> \bar{n}_{dc} + \bar{p}_{dc}$, where the modulated photocurrent is controlled by trapping and release processes, and
- case (ii), $\omega << \bar{n}_{dc} + \bar{p}_{dc}$, where the modulated photocurrent is controlled by recombination.

These two cases naturally define the so-called high frequency regime and low frequency regime of the modulated photocurrent experiment.

2.3.1 High frequency regime (HF-MPC)

In the high frequency regime, it can be demonstrated that the system (2.37) can be split into two independent linear subsystems

$$\begin{pmatrix} A_n & B_n \\ -B_n & A_n \end{pmatrix} \begin{pmatrix} n_i \\ n_r \end{pmatrix} = \begin{pmatrix} 0 \\ G_{ac} \end{pmatrix} \quad , \qquad (2.47)$$

and

$$\begin{pmatrix} A_p^* & B_p^* \\ -B_p^* & A_p^* \end{pmatrix} \begin{pmatrix} p_i \\ p_r \end{pmatrix} = \begin{pmatrix} 0 \\ G_{ac} \end{pmatrix} \quad , \qquad (2.48)$$

where it can be noticed that Eq. (2.48) is the transformed of Eq. (2.47) by the operator $\mathcal{F}$. This separation into two sub-systems indicates that, as far as the alternating contribution is concerned, the populations of electrons and holes are disconnected in the HF regime and can be found separately from the resolution of each subsystem. If we define two quantities, Num_n and Den_n, by

$$Num_n = \frac{B_n \mu_n}{A_n^2 + B_n^2} \quad , \qquad (2.49)$$

and

$$Den_n = \frac{A_n \mu_n}{A_n^2 + B_n^2} \quad , \qquad (2.50)$$

and two equivalent quantities Num_{p}^{*} and Den_{p}^{*}, using the transformation $\mathcal{F}$ of Num_{n} and Den_{n}, respectively, the phase shift and the modulus of the alternating photocurrent can be obtained from

$$\tan(\phi) = \frac{Num_{\mathrm{n}} + Num_{\mathrm{p}}^{*}}{Den_{\mathrm{n}} + Den_{\mathrm{p}}^{*}} \quad , \qquad (2.51)$$

and

$$|I_{\mathrm{ac}}| = G_{\mathrm{ac}} Sq\xi \sqrt{\left(Num_{\mathrm{n}} + Num_{\mathrm{p}}^{*}\right)^{2} + \left(Den_{\mathrm{n}} + Den_{\mathrm{p}}^{*}\right)^{2}} \quad , \qquad (2.52)$$

which are general expressions for $\tan(\phi)$ and $|I_{\mathrm{ac}}|$ including the contributions of both electrons and holes.

These expressions can be simplified when one considers that one type of carrier is predominant. For instance, if the inequalities $Num_{\mathrm{n}} >> Num_{\mathrm{p}}^{*}$ and $Den_{\mathrm{n}} >> Den_{\mathrm{p}}^{*}$ are satisfied (electron-controlled behavior), the expressions (2.44)-(2.45) can be simplified into those given by Oheda [11]

$$\tan(\phi) \approx \frac{B_{\mathrm{n}}}{A_{\mathrm{n}}} \quad , \qquad (2.53)$$

and

$$|I_{\mathrm{ac}}| \approx \frac{G_{\mathrm{ac}} Sq\xi}{\sqrt{A_{\mathrm{n}}^{2} + B_{\mathrm{n}}^{2}}} \quad . \qquad (2.54)$$

With simplified expressions of A_{n} and B_{n} (See [36]), assuming that the energy dependence of the DOS is weaker than that of $\exp(|E|/k_{\mathrm{B}}T)$, Eqs. (2.53) and (2.54) lead to

$$\frac{N(E_{\omega \mathrm{n}})C_{\mathrm{n}}}{\mu_{\mathrm{n}}} = \frac{2}{\pi k_{\mathrm{B}} T} Sq\xi G_{\mathrm{ac}} \frac{\sin\phi}{|I_{\mathrm{ac}}|} \quad , \qquad (2.55)$$

where, following Eq. (2.46), $E_{\omega \mathrm{n}}$ is given by

$$E_{\mathrm{C}} - E_{\omega \mathrm{n}} = k_{\mathrm{B}} T \ln\left(\frac{C_{\mathrm{n}} N_{\mathrm{C}}}{\omega}\right) \quad . \qquad (2.56)$$

These two equations, from which it is possible to achieve a DOS spectroscopy, were also proposed by R. Brüggemann and co-workers [35] in their treatment of the MPC experiment. The same type of equations can be obtained in the case where the alternating photocurrent is dominated by holes, using the $\mathcal{F}$ transformation (N_{C} being transformed into N_{V}).

At this stage, some important points have to be underlined. First, Eqs. (2.55) and (2.56) are only valid if $\omega >> \bar{n}_{\mathrm{dc}} + \bar{p}_{\mathrm{dc}}$. Comparing Eqs. (2.46) and (2.25), this inequality implies that the probed energy $E_{\omega \mathrm{n}}$ is above the quasi Fermi level for trapped electrons E_{tn}, meaning that the probed energy is in the range of trapping and release (as opposed to recombination) energies defined by the DC steady-state conditions. In the case of a predominant hole contribution, this inequality means that the probed energy $E_{\omega \mathrm{p}}$ is below the quasi Fermi level for trapped holes E_{tp}. E_{F0} being the equilibrium Fermi level, we can define a level E_{F0}^{*} by $e_{\mathrm{n}}(E_{\mathrm{F0}}^{*}) = e_{\mathrm{p}}(E_{\mathrm{F0}})$ if the material is p-type, or by $e_{\mathrm{p}}(E_{\mathrm{F0}}^{*}) = e_{\mathrm{n}}(E_{\mathrm{F0}})$ if the material is n-type, meaning that E_{F0}^{*} is roughly symmetrical to E_{F0} with respect to mid-gap. From the above remark, we can conclude that the defect states located in the energy range in between E_{F0} and $E_{\mathrm{F0}}{}^{*}$ can never be probed in the high frequency regime of the modulated photocurrent. As a

consequence, a DOS spectroscopy from HF-MPC is only possible in materials that are not highly doped. For highly doped materials, only a limited energy range could be accessible, and, in addition, such materials have a high dark conductivity and generally a poor light sensitivity, which also lead to signal-to-noise ratio issues.

Second, the absolute values of the density of states cannot be obtained straightforwardly, unless the capture cross-section of the probed states and the extended states mobility are known. However, a relative DOS spectrum can be deduced, the quantity NC/μ, since the quantities in the right-hand side of Eq. (2.55) are known or extracted from the experiment. Furthermore, using an incorrect value of the attempt-to-escape frequency $\nu_n = C_n N_C$ (or $\nu_p = C_p N_V$ in case of a hole predominant contribution) leads to a distortion of the spectrum, since, according to Eq. (2.56), the energy is then not properly scaled.

Finally, according to Eq. (2.56) the range of explored energies depends linearly on the sample temperature and logarithmically on ω. Theoretically, it could be possible to explore a large range of energies with a very large range of frequencies. However, from an experimental point of view the available range of ω is limited by the bandwidth of the apparatus used to amplify and to record the alternating photocurrent. That is why, in our experimental setup, the frequencies of the modulation $f = \omega/2\pi$ are chosen in between 1 Hz and 40 kHz, and the explored energy range is extended by playing with the sample temperature.

2.3.2 Low frequency regime (LF-MPC)

Fig. 2.5 illustrates the traffic of carriers between extended states and the two characteristic levels $E_{\omega p}$ and $E_{\omega n}$ in a-Si:H for the low frequency regime of the MPC experiment. In this regime these levels are located between the limits of the recombination zone defined by E_{tp} and E_{tn}. Hence, the probed energy is located in the recombination zone. In this case, the system (2.37) cannot be split into two independent subsystems and it has to be solved completely to obtain the expressions of n_r, n_i, p_r, p_i and eventually deduce the expression of $\tan(\phi)$. Since this regime corresponds to $\omega << \bar{n}_{dc} + \bar{p}_{dc}$, we can write $\omega\tau << 1$ and, in a first order approximation, it can be shown that $|I_{ac}| = Sq\xi G_{ac}(\mu_n\tau_n + \mu_p\tau_p)$ and $\phi = 0$ [36]. However, if one develops $\omega\tau$ to the second order in a Taylor expansion it is possible to calculate an expression of $\tan(\phi)$ as function of the transport parameters of the material, to end with

$$\frac{\tan\phi}{\omega} = \frac{\bar{n}_{dc}\mu_n\tau_n N_n\left[(G_{dc}+\bar{p}_{dc}N_p)^2+\bar{p}_{dc}^2N_p^2\right]+\bar{p}_{dc}\mu_p\tau_p N_p\left[(G_{dc}+\bar{n}_{dc}N_n)^2+\bar{n}_{dc}^2N_n^2\right]}{2G_{dc}(\bar{n}_{dc}+\bar{p}_{dc})(G_{dc}+\bar{n}_{dc}N_n+\bar{p}_{dc}N_p)\left[\mu_n\tau_n(G_{dc}+\bar{p}_{dc}N_p)+\mu_p\tau_p(G_{dc}+\bar{n}_{dc}N_n)\right]} \quad , \qquad (2.57)$$

in which $N_n = k_B T\, N(E_{tn})$ and $N_p = k_B T\, N(E_{tp})$. Details of this theoretical development were presented in Ref. [41].

According to Eq. (2.57), $\tan(\phi)$ depends on the density of states at the quasi Fermi levels for trapped carriers via N_n and N_p, on DOS integrals via τ_n and τ_p, on capture cross sections of the states via $\bar{n}_{dc}$ and $\bar{p}_{dc}$, and on the carriers mobilities. Therefore, a determination of the DOS is hardly possible. However, depending on the studied material properties, Eq. (2.57) can be simplified. First, if the quasi Fermi levels for trapped carriers are more than a few $k_B T$ away from the dark Fermi level and if the DOS does not depend too strongly on energy, it can be shown from charge neutrality that $G_{dc} >> \bar{n}_{dc}N_n$ and $G_{dc} >> \bar{p}_{dc}N_p$, and Eq. (2.57) simplifies into

$$\frac{\tan\phi}{\omega} = \frac{\bar{n}_{dc}\mu_n\tau_n N_n+\bar{p}_{dc}\mu_p\tau_p N_p}{2G_{dc}(\bar{n}_{dc}+\bar{p}_{dc})(\mu_n\tau_n+\mu_p\tau_p)} \quad . \qquad (2.58)$$

In addition, if we assume that the electrons are the majority carriers giving the major contribution to both the DC current ($\mu_n \tau_n >> \mu_p \tau_p$) and the capture rate ($\bar{n}_{dc} >> \bar{p}_{dc}$), we obtain a very simple expression:

$$N(E_{tn}) = \frac{2G_{dc}}{k_B T} \frac{\tan \phi}{\omega} \quad . \qquad (2.59)$$

Other authors have found expressions of the same form:

$$N(E_{tn}) = \frac{KG_{dc}}{k_B T} \frac{\tan \phi}{\omega} \quad . \qquad (2.60)$$

with $K = 1/\ln(2)$ for R. R. Koropecki *et al.* [42], and $K = 1$ for P. Kounavis [43], instead of $K = 2$ in our analysis. These differences can be attributed to the various approximations used to derive an analytical expression for the DOS reconstruction. Numerical calculations have shown that $K = 2$ leads to more accurate reconstruction of the DOS [41].

To achieve a DOS spectroscopy based on Eq. (2.59) it is necessary to know the position of the quasi Fermi level for trapped electrons. In the case where $\bar{n}_{dc} >> \bar{p}_{dc}$, the quasi Fermi level for trapped electrons coincides with the quasi Fermi level for free electrons, which can be estimated from the DC current I_{dc}

$$E_C - E_{tn} \approx E_C - E_{Fn} = k_B T \ln\left(\frac{\mu_n N_C S q \xi}{I_{dc}}\right) \quad . \qquad (2.61)$$

The position of the quasi Fermi level can be changed either by changing the flux at a constant temperature or by changing the temperature at a constant flux. The first technique would need very high fluxes to cover a high range of energies. The second technique may lead to erroneous results if the mobility or the capture coefficient depends on temperature and if such dependence is unknown. However, usually this temperature dependence is weak compared with the exponential dependence on energy of the emission frequencies. Therefore, we favor the use of temperature variations with a reasonable flux to achieve a DOS spectroscopy in a wide energy range in the LF-MPC.

An interesting point is that the deduced value of $N(E_{tn})$ in the LF-MPC does not depend on any unknown parameter such as mobility and capture coefficient. On the other hand, the energy scaling depends on the product $\mu_n N_C$. Considering the MPC technique in the high frequency regime, one obtains the exact values of NC/μ with an energy scaling linked to the attempt-to-escape frequency $C_n N_C$. It is easy to understand that, if the two techniques are used to probe the DOS in the same energy range, the HF-MPC DOS must coincide with the LF-MPC DOS. Thus, the ratio μ/C can be determined so as to match the results of both experiments. In the case where N_C is known, this could even lead to the determination of μ and C independently.

Finally, we would like to underline that the above ideal situation may be compromised either when the transport parameters present some extreme values [41] or when many different species of states are present in the gap [30].

2.3.3 Summary of the two MPC regimes

The physics that governs the two regimes of MPC is recalled in Fig. 2.5, where a DOS typical of a-Si:H has been used as an illustration. The same DC conditions are assumed in both parts of the figure, setting E_{tp} and E_{tn} and determining the recombination zone.

In the HF regime, the two levels $E_{\omega p}$ and $E_{\omega n}$ at which the emission frequency (of holes towards the valence band, and of electrons towards the conduction band, respectively) coincides with the angular frequency of the MPC, are outside the recombination zone. The phase shift of the MPC is

then primarily determined by the trapping and emission processes at these states. Information on these states is extracted from the analysis of MPC presented in §2.3.1.

In the LF regime, the two levels $E_{\omega p}$ and $E_{\omega n}$ are in the recombination zone and do not play a dominant role anymore, because the MPC is determined by recombination processes. Information on the states at the characteristic energies of the recombination zone, E_{tp} and E_{tn}, can thus be obtained from the analysis of MPC presented in §2.3.2.

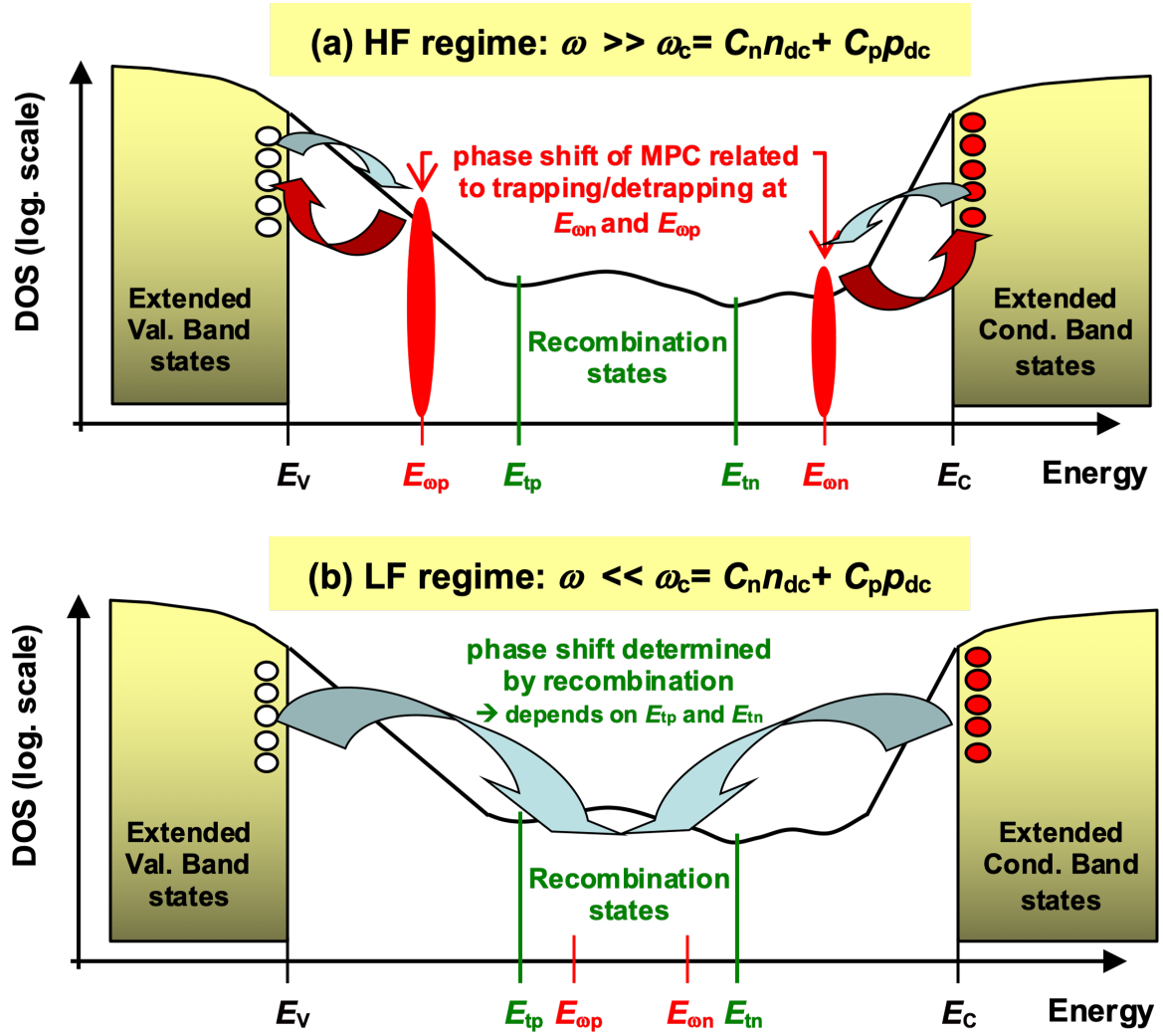

Fig. 2.5. Illustration of the two regimes of the MPC experiment under the same DC illumination conditions that determine the zone of recombination states delimited by the quasi Fermi levels for trapped holes and electrons, E_{tp} and E_{tn}, respectively. In the high frequency regime (also called trapping-and-release regime) of MPC (a), the trapping and release events at $E_{\omega p}$ and $E_{\omega n}$, which are located outside the recombination zone, play a major role in the MPC phase shift, which allows one to extract properties of the states at $E_{\omega p}$ or $E_{\omega n}$, depending on whether holes or electrons give the predominant contribution to MPC. In the low frequency regime, (also called recombination regime) of MPC (b), $E_{\omega p}$ and $E_{\omega n}$ are in the recombination zone and do not act anymore as trapping-and-release states. The MPC is then determined by recombination events and properties of the states at E_{tp} or E_{tn} can be extracted.

Table 2.2 summarizes the equations to be used to reconstruct the DOS when the MPC is performed in the HF or LF regime, as well as the approximations used to determine the reconstruction and the conditions under which each of the experiment has to be performed.

Table 2.2. Comparison of the HF and LF regimes of the MPC.

	High frequency regime	Low frequency regime
DOS reconstruction	$k_B T \frac{C_n N(E_{\omega n})}{\mu_n} \approx \frac{2}{\pi} Sq\xi G_{ac} \frac{\sin\phi}{I_{ac}}$	$N(E_{tn}) \approx \frac{2G_{dc}}{k_B T} \frac{tan\phi}{\omega}$
Energy scale	$E_C - E_{\omega n} \approx k_B T \, ln\left(\frac{C_n N_C}{\omega}\right)$	$E_C - E_{tn} \approx k_B T \ln\left(\frac{\mu_n N_C Sq\xi}{I_{dc}}\right)$
Required approximations	$\frac{C_n N(E_{\omega n})}{\mu_n} << \frac{C_p N(E_{\omega p})}{\mu_p}$	$\mu_n n_{dc} >> \mu_p p_{dc}$ $C_n n_{dc} >> C_p p_{dc}$
Parameters needed for reconstruction	$\frac{C_n}{\mu_n}$ and $C_n N_C$	$\mu_n N_C$
Experimental constraints	Limited frequency range	Limited DC generation rate, very low phase shifts

2.3.4 Illustration by means of simulations

In this part we shall illustrate some of the key points of the MPC experiment by means of numerical calculations.

We start with a very simple density of states, the same as we have used in §2.2.3, and we have chosen the same capture coefficients for all the states $C_n = C_p = 2\times10^{-8}$ cm^{3}s^{-1}. The MPC experiment was simulated using 21 frequencies for the modulation, in a range from $f_1 = 12$ Hz to $f_{21} = 39.9$ kHz such that $f_{i+1} = 1.5\times f_i$, and for temperatures in a range from 100 to 460 K with a 20-K step. To work with a 'sample' in which one type of carrier is clearly dominant, we have chosen values of the extended states mobilities equal to $\mu_n = 10$ cm^{2}V^{-1}s^{-1} and $\mu_p = 0.1$ cm^{2}V^{-1}s^{-1}. For each temperature, the DC values of the carrier densities and of the current are first calculated, then the AC values are calculated, in particular the modulus and the phase shift of the MPC, from which the NC/μ spectra are reconstructed according to Eqs. (2.55)-(2.56) and compared to the one introduced in the simulation.

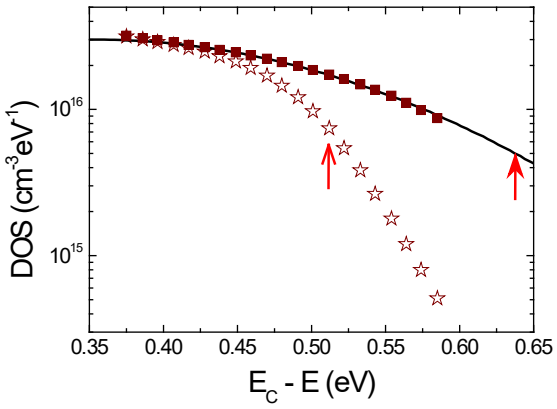

Fig. 2.6. Reconstructed DOS from the NC/μ spectra deduced from Eqs. (2.55)-(2.56) applied to the results of calculations performed with $G_{dc} = 10^{15}$ cm^{-3}s^{-1} (squares) and $G_{dc} = 10^{18}$ cm^{-3}s^{-1} (stars) at a temperature of 300 K. The arrows indicate the position of E_C - E_{tn}. The full line corresponds to the introduced DOS. Each reconstructed DOS displays 21 points corresponding to the 21 frequencies used in the MPC calculation.

In Fig. 2.6 we present an example of DOS reconstruction from calculations performed at T = 300 K at two DC generation rates: $G_{dc} = 10^{18}$ cm^{-3}s^{-1} (stars) and $G_{dc} = 10^{15}$ cm^{-3}s^{-1} (squares). The 21 reconstructed data points correspond to the 21 frequencies. The arrows in the figure indicate the

energy corresponding to the quasi Fermi level of trapped electrons, $E_C - E_{tn}$ = 0.52 eV and $E_C - E_{tn}$ = 0.64 eV, for $G_{dc} = 10^{18}$ cm^{-3}s^{-1} and $G_{dc} = 10^{15}$ cm^{-3}s^{-1}, respectively. The DOS probed at these energies corresponds to an angular frequency $\omega = \bar{n}_{dc} + \bar{p}_{dc}$, which defines the transition angular frequency between the HF and LF regimes. At the lowest flux we can observe that the reconstructed DOS nicely matches the introduced one because the angular frequencies we used are all such that $\omega >> \bar{n}_{dc} + \bar{p}_{dc}$. For the highest flux we obtain a good match only for $E_C - E < 0.43$ eV because the condition $\omega >> \bar{n}_{dc} + \bar{p}_{dc}$ is fulfilled only at the highest frequencies. A strong deviation of the reconstructed DOS compared to the introduced one appears at $E_C - E > 0.47$ eV, because these points are reconstructed for frequencies such that ω is of the order of or even lower than $\bar{n}_{dc} + \bar{p}_{dc}$, a frequency range where the Eqs. (2.55)-(2.56) are not valid.

In Fig. 2.7 we show the whole set of reconstructed DOS data at all probed frequencies and temperatures, and for two values of the DC generation rate: G_{dc}, 10^{15} cm^{-3}s^{-1} (squares) and 10^{18} cm^{-3}s^{-1} (stars). The trend observed in Fig. 2.6 for the highest DC generation rate is confirmed. For the calculation performed at the lowest frequencies and the highest flux we observe for each temperature a 'tail' that departs from the original DOS, and that corresponds to the fact that the probed states at these frequencies are located below the quasi Fermi level for trapped electrons, *i.e.* $\omega < \bar{n}_{dc} + \bar{p}_{dc}$. As the temperature is decreased while maintaining a constant DC generation rate (constant DC flux), the recombination zone enlarges and E_C - E_{tn} moves toward lower energy values. However, the spectra are gathering and match the introduced DOS when the calculation is performed at the highest frequencies, where the condition $\omega >> \bar{n}_{dc} + \bar{p}_{dc}$ is fulfilled. For the lowest generation rate, it can be emphasized that the spectra calculated for each temperature are gathering altogether and describe the introduced density of states, except when the probed states are located below the dark Fermi level. This behavior confirms the ability of the MPC technique to probe the DOS of a semiconductor with the exception of the energy range located between E_{F0} and E^*_{F0}, the symmetrical of E_{F0} with respect to mid-gap.

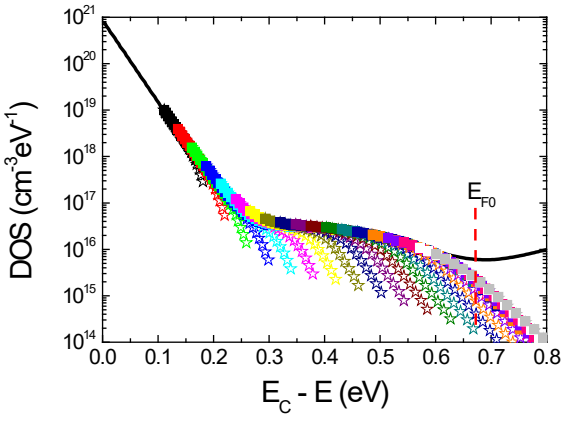

Fig. 2.7. Reconstructed DOS from the *NC*/μ spectra deduced from Eqs. (2.55)-(2.56) applied to the results of calculations performed with $G_{dc} = 10^{15}$ cm^{-3}s^{-1} (squares) and $G_{dc} = 10^{18}$ cm^{-3}s^{-1} (stars) for temperatures ranging from 100 K to 460 K with a 20-K step represented by different colors. For each temperature, there are 21 data symbols corresponding to the 21 frequencies as in Fig. 2.6. The reconstructed spectra are compared to the introduced DOS (full line). The vertical dashed line indicates the position of the dark Fermi level E_{F0}.

Another interesting point to underline is the influence of the transport parameters on the DOS determination. Theoretically, we expect to probe the DOS for states exchanging carriers with the conduction band if the electrons are predominant in the modulated photocurrent, or with the valence band if the holes provide the largest contribution to the modulated photocurrent. From the previous simulation it can be seen that, with the chosen parameters, the MPC experiment probes the electron trapping states. We have performed another calculation, at a constant generation rate of $G_{dc} = 10^{18}$ cm^{-3}s^{-1}, exchanging the values of the extended states mobilities, *i.e.* taking $\mu_n = 0.1$ cm^{2}V^{-1}s^{-1} and $\mu_p = 10$ cm^{2}V^{-1}s^{-1}. The reconstructed spectra in the two cases, μ_n/μ_p = 10/0.1 and μ_n/μ_p = 0.1/10, are displayed in Fig. 2.8.

It can be clearly seen that, in the case where the holes give the major contribution to the modulated photocurrent with $\mu_p >> \mu_n$, the probed DOS is that of the states exchanging holes with the valence band (open circles), *i.e.* here the valence band tail. It can be further confirmed that the states located between E_{F0} and E^*_{F0} cannot be probed by the MPC technique.

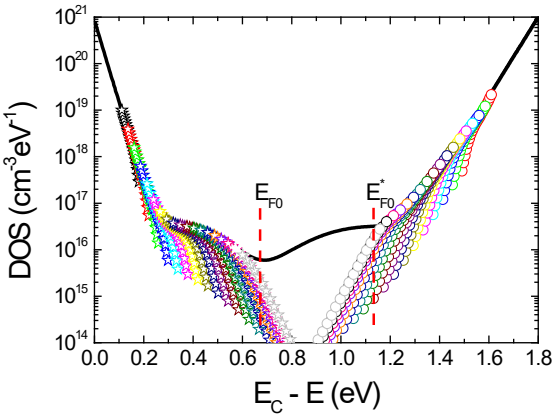

Fig. 2.8. Influence of the predominance of electrons or holes in the MPC experiment by changing the mobility ratios. The DOS is reconstructed from the NC/μ spectra in two cases: predominance of electrons (stars, μ_n/μ_p = 10/0.1), and predominance of holes (circles, μ_n/μ_p = 0.1/10). Calculations were performed with $G_{dc} = 10^{18}$ cm^{-3}s^{-1}. Both reconstructions are compared to the introduced DOS (full line).

To explain why the probed states can be either those exchanging electrons with the conduction band or those exchanging holes with the valence band, we can define an MPC trap-controlled mobility. In many semiconductors, particularly in the amorphous ones, there is always a competition between trapping/release and transport of carriers. Concerning trapping, the quantity $k_BTN(E_\omega)C$ corresponds to the capture rate of localized states in a k_BT range of energies around E_ω, which, from its definition, is the energy where the emission rate equals ω. The competition mentioned above is therefore described by the quantity

$$\mu(\omega) = \frac{\mu\,\omega}{k_B T\, N(E_\omega)\, C} \quad , \qquad (2.62)$$

from which it is easy to understand that, for a given ω, the MPC will be controlled by carriers presenting the highest trap-controlled mobility $\mu(\omega)$, that is the lowest NC/μ value.

It can be also noted from Fig. 2.8 that, whatever the carriers controlling the MPC current, the MPC spectra always present 'tails' that depart from the true DOS due to the influence of the flux on the position of the quasi Fermi levels, if the chosen flux is sufficiently high. In addition, it is also apparent that, as theoretically predicted, the states located between the dark Fermi level E_{F0} and its symmetrical with respect to mid gap E^*_{F0} cannot be probed by the MPC technique.

Concerning the implementation of the experiment in the low frequency regime, we must underline that the experimental conditions have to be chosen appropriately to obtain an accurate reconstruction of the DOS from the experimental data. Indeed, the DOS determination from Eq. (2.59) is based on the measurement of low phase shifts at low frequencies. For this purpose, the sample must be uniformly illuminated in its whole thickness. This last point may not be fulfilled for a sample too thick and/or having a high absorption coefficient. Fig. 2.9 displays the free electron distribution in the thickness of a 2 µm thick undoped a-Si:H thin film with two different absorption coefficients: $\alpha = 10^5$ cm^{-1} and $\alpha = 10^4$ cm^{-1}. The DC flux was taken equal to $F_{dc} = 10^{15}$ cm^{-2}s^{-1}. It can be seen that, with the highest α, the electron distribution is highly non-uniform. With 2-D calculations taking account of the generation in the depth of the material it was shown by R. Lachaume *et al.* [44] that, in this case, even though the diffusion of carriers may contribute to some homogenization of the carrier distribution, the LF-MPC regime is not reached in the whole material. This is illustrated in Fig. 2.9 where the electron concentration defining the limit between the HF and LF regimes, given by $\omega_c = C_n n + C_p p \approx C_n n$, is indicated for a modulation frequency f_c = 50 Hz as a horizontal dashed line. As a consequence, the

phase shift values are larger compared to that one would obtain if the LF-MPC regime would be reached in the whole layer thickness, and this can lead to a large overestimation of the DOS. Such an example is shown in Fig. 2.10, where the application of Eqs. (2.59) and (2.61) leads to significantly larger values and distortion in the DOS shape compared to the actual DOS introduced in the calculation.

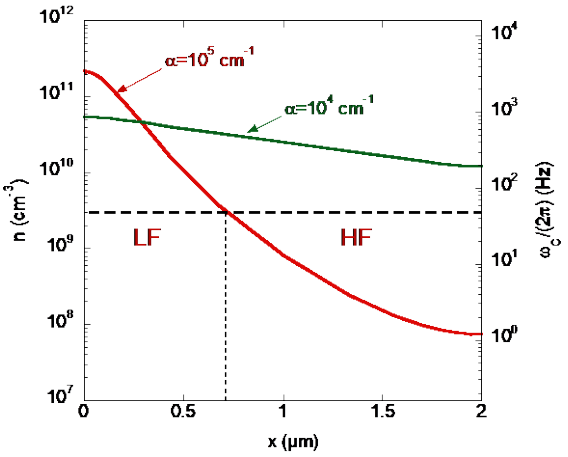

Fig. 2.9. Calculation with two absorption coefficients of the free electron distributions generated by a DC flux of 10^{15} $cm^{-2}s^{-1}$ in the thickness of a 2 µm thick undoped a-Si:H thin film. The horizontal dashed line indicates the electron concentration for which one reaches the limit between HF and LF regimes, given by $\omega_c \approx C_n n$ for a modulation frequency of 50 Hz.

On the other hand, the reconstruction of the DOS in the HF-MPC regime was shown to be almost insensitive to the non-uniformity of the generation [44]. However, in both cases it is difficult to define the area S through which the current is flowing, because the effective penetration depth is unknown. In conclusion, these findings indicate that the MPC experiment must be performed with a light having a photon energy only slightly higher than the band gap, to give rise to a band-to-band generation but to be absorbed as deep and homogeneously as possible. Also, particularly in the case of LF-MPC, it should be performed with a thin sample, a high flux and a low frequency of the modulation so that the LF-MPC regime is reached in the whole thickness of the sample, as it is the case in Fig. 2.9 for a low absorption coefficient ($\alpha = 10^4$ cm^{-1}).

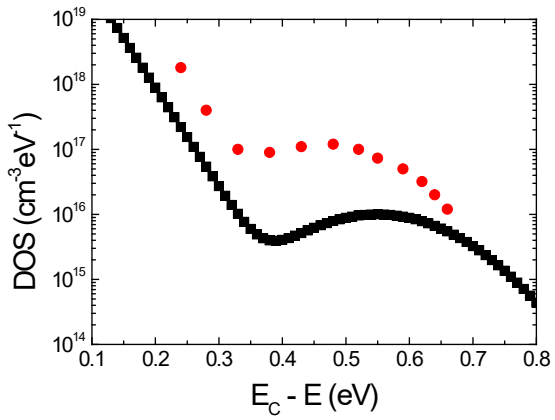

Fig. 2.10. Example of DOS reconstructed using the LF-MPC equations (2.59) and (2.61) for a 2D calculation of the photocurrent where the distribution of free carriers is strongly non homogeneous as for $\alpha = 10^5$ cm^{-1} in Fig. 2.9 (red circles), compared to the DOS introduced in the calculation (black squares). Adapted from Ref. [44].

Before presenting experimental results, we have to underline that, for the sake of clarity, the theoretical developments and numerical calculations have been presented here for the very simple case of monovalent states. Nevertheless, they can also be applied to distributions of states obeying different statistics, such as amphoteric states. These defects are characterized by three states of charge: negative (D^-), neutral (D^0) and positive (D^+), and do not follow the usual Fermi-Dirac statistics. In a-Si:H they are linked to deep defects created by dangling bonds and their distribution in the gap was theoretically calculated from the defect-pool model [45]. Concerning the MPC technique, theoretical developments taking the peculiar statistics of these states have been presented in [46], where all the trends exposed in the case of monovalent states were also found in the case of amphoteric states.

2.3.5 Experimental results

Thanks to the versatility of the MPC experiment, it can be (and indeed it was) applied to a large variety of materials, from thin films to bulk crystalline semiconductors. Since it was developed for the study of a-Si:H, many publications have been devoted to this material and to polymorphous hydrogenated silicon (pm-Si:H) thin films, either undoped or doped with erbium or boron [47, 48]. It was also applied for investigations on other types of thin films such as micro or poly crystalline silicon, CIGS, As_2Se_3 and Sb_2S_3 [35, 49 - 51]. The MPC technique was also used to investigate on the properties of bulk crystalline materials, such as phase change materials (GeTe, GeSnTe) [52, 53], photorefractive materials (BTO, CdTe) [54, 55], and semi-insulating crystals (GaAs, SiC) [56, 57].

2.3.5.a *Application to a crystalline material*

As an example, we present results obtained on semi-insulating chromium doped gallium arsenide, GaAs:Cr. The samples, 400 µm thick, were cut from an ingot grown in the <110> direction by the liquid encapsulated Czochralski method at the Institute of Electronic Materials Technology (ITME, Warsaw, Poland). Coplanar and ohmic AuGe-Ni electrodes were deposited on top of the polished wafers with a gap of 0.8 mm. The applied bias was varied in the range 2-50 V and the illumination was provided by an infra-red LED (850 nm), the photon energy of which (1.46 eV) is just above the GaAs band gap (~ 1.43 eV). A low DC flux of 2×10^{12} $cm^{-2}s^{-1}$ was chosen to ensure that the experiment was performed in the HF regime. The temperature was varied in the range 78 - 339 K in 3-K steps and the frequency of the modulation was varied between 12 Hz and 39.9 kHz, such that $f_{i+1} = 1.5\times f_i$ (For details see [56]).

Fig. 2.11 shows the spectra reconstructed from the experimental MPC data. For clarity, only the spectra recorded each 6 K are displayed. In a first step, the energy scaling was achieved assuming a constant attempt-to-escape frequency of $\nu_a = 10^{12}$ s^{-1}. The reader may note that the energy scaling is labeled $|E_{be} - E|$, where E_{be} stands for the energy of the band edge, since we do not know if we are probing electron or hole trapping states. Several peaks are clearly visible, a situation completely different from that encountered with the smoothly varying DOS of a-Si:H.

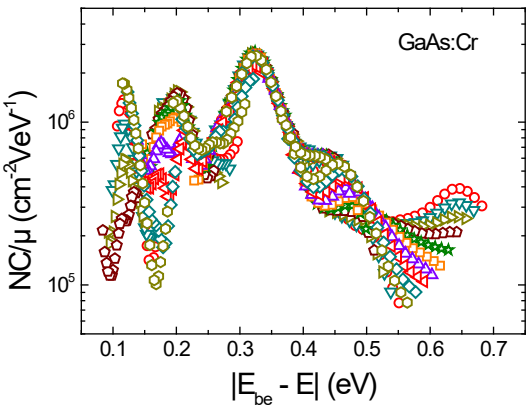

Fig. 2.11. Experimental NC/μ spectra reconstructed from the HF-MPC technique applied to a GaAs:Cr sample. Each set of symbols corresponds to a given temperature and each symbol to a given frequency. The energy scale was fixed assuming a constant attempt-to-escape frequency $\nu_a = 10^{12}$ s^{-1}.

Each peak should correspond to a peculiar trap level and we have proposed several methods to determine the attempt-to-escape frequency and the energy position of a given peak [56]. One of them is based on the study of the maximum of the peaks. Since the experiment is performed in 3 K steps, a given peak is described by several MPC spectra. For each spectrum the maximum is obtained at a temperature-dependent frequency f_{max}. The energy position of the peak, E_{max}, is related to f_{max} through Eq. (2.56) in which $E_{\omega n}$, ω and C_nN_C are replaced by E_{max}, $2\pi f_{max}$, and the attempt-to-escape frequency ν_a, respectively. Taking account of a T^2 dependence of ν_a (due to the temperature dependence of the

thermal velocity and effective DOS in the conduction and valence bands), an Arrhenius plot of T^2/f_{max} should yield a straight line the slope of which gives the activation energy corresponding to the energy position of the peak. Such plots are presented in Fig. 2.12, from which five different peaks can be clearly identified.

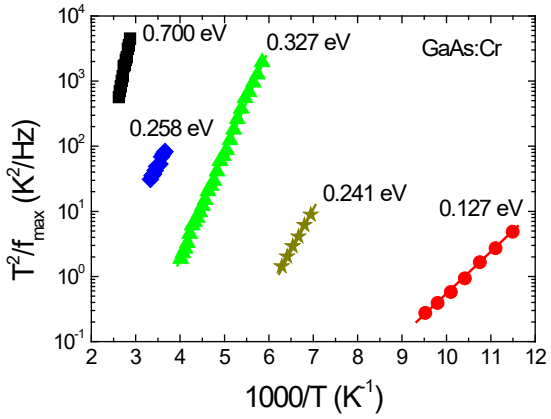

Fig. 2.12. Arrhenius plots of T^2/f_{max} for different peaks observed in Fig. 2.11. The energy positions of the different peaks, given by the activation energy deduced from the slope of each set of points, are indicated in the figure.

From the peak position, the attempt-to-escape frequency can be deduced by adjusting it until all the MPC spectra describe the peak properly. In addition, if the mobility values are known, the order of magnitude of the defect concentration can be obtained from the quantity NC/μ. As an example, we may consider the peak located at $E_{max} \approx 0.33$ eV, the highest one in the center of Fig. 2.11. The best match between the MPC spectra describing this peak is obtained with an attempt-to-escape frequency at 300 K $\nu_{300} = 1.2\times10^{12}$ s^{-1}. With these values for E_{max} and ν_{300}, it can be reasonably identified as the EL6 level according to the literature [58]. The electronic mobility was estimated to be of the order of 5000 cm^{2}V^{-1}s^{-1}. Therefore, the peak density can be plotted with this value, using ν_{300} to scale the energy, to give a Gaussian shape distribution with a maximum of $N \approx 5\times10^{15}$ cm^{-3}eV^{-1} and a standard deviation of the order of 0.05 eV, from which we deduce a defect concentration of 6.3×10^{14} cm^{-3} in good agreement with the 5.6×10^{14} cm^{-3} estimated in as-grown semi-insulating GaAs by K. Yasutake and coworkers [59].

Some other levels are more difficult to reveal because they do not present a well-defined maximum as, for instance, the shoulder present in the 0.4-0.5 eV range of Fig. 2.11. However, for a given structure described by several MPC spectra, all these spectra must superimpose to describe the same DOS provided the attempt-to-escape frequency is correctly chosen for the energy scaling. In the case of the shoulder in the range 0.4-0.5 eV, we have found that a good order of magnitude for ν_a at 300 K was $\nu_{300} = 10^{10}$ s^{-1}, leading to a peak position of the order of 0.34-0.35 eV. The determination of these parameters is less precise than when a clear maximum is observed, still, rather good estimates can be obtained.

2.3.5.b *Application to amorphous thin films*

The methods proposed to extract transport parameters from the MPC results when this technique is applied to crystalline materials cannot be applied to amorphous thin films because the DOS distributions are large and do not exhibit any peak. However, by combining the data obtained from HF-MPC, LF-MPC and SSPC, a lot of information can be gained on the transport properties of thin film semiconductors.

Here we illustrate the use of these three techniques on a polymorphous hydrogenated silicon thin film (pm-Si:H) prepared by radio frequency powered plasma enhanced chemical vapor deposition (RF-PECVD) at 423 K from a mixture of hydrogen and silane (97 % H_2, 3 % SiH_4) at a high pressure (1.4 Torr) and high RF power (110 mW/cm^2). The film, ~ 1µm thick, deposited on glass, was fitted

with parallel electrodes, 1.5 mm apart, and annealed at 450 K under vacuum (10^{-5} mbar) before measurements.

To perform the LF-MPC under conditions as close as possible to the optimum ones (see Fig. 2.9) the sample was illuminated by red LEDs (650 nm, $\alpha \approx 10^4$ cm^{-1}) with a DC flux of 3×10^{15} cm^{-2}s^{-1} and an AC flux 3 times lower in intensity and modulated in the range 1-300 Hz. The temperature was varied in the range 100-450 K in 10-K steps. The HF-MPC was achieved with the same red light with a DC flux of 10^{13} cm^{-2}s^{-1} and an AC flux 3 times lower. The frequencies of the modulation were in the range 12 Hz – 40 kHz and the temperature was varied in the range 120 K - 450 K in 30-K steps. The SSPC measurements were done with the same LEDs with a flux ranging from 1.5×10^{13} to 3×10^{15} cm^{-2}s^{-1} varied in a 1-2-5 scale ($1\times1.5\times10^{13}$, $2\times1.5\times10^{13}$, $5\times1.5\times10^{13}$, …). The γ coefficient was calculated from Eq. (2.4) each 10-K, in the same range of temperature as the LF-MPC, by measuring two DC currents at each generation rate G_{dc} and at $G_{dc}\times1.2$. All the experimental details can be found in [60].

In Fig. 2.13 we present the results obtained on this pm-Si:H sample, where the NC/μ spectra have been plotted according to Eqs. (2.26), (2.27), Eqs. (2.55), (2.56), and Eqs. (2.59), (2.61) from the SSPC, HF-MPC, and LF-MPC data, respectively.

To deduce the DOS and some of the transport parameters we have first adjusted the HF-MPC-NC/μ and LF-MPC-NC/μ in the CBT region. Indeed, at low temperature one may consider that only one species of states is probed by these two experiments: the CBT states. From this adjustment we deduce the quantities $\mu_n N_c$ and $C_n N_c$, fixing the energy scales of the LF-MPC- and HF-MPC-NC/μ, respectively. Then, these values have been applied to all the data, in particular to the energy scale of the γ-NC/μ (Eq. (2.27)), even when they may be inappropriate to plot the LF-MPC and HF-MPC-NC/μ distributions as for the deep states since their capture coefficients may be different from those of the CBT.

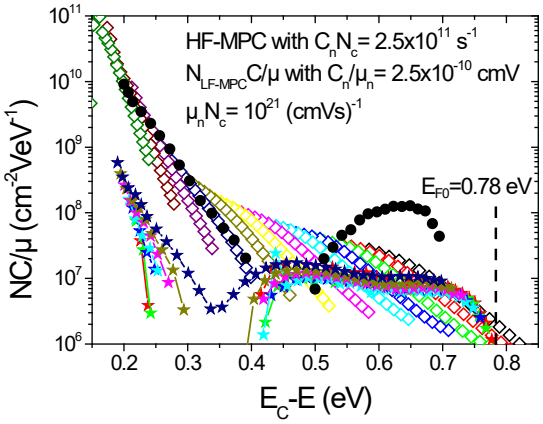

Fig. 2.13. Comparison of different NC/μ spectra coming from three different experiments performed on a pm-Si:H sample: HF-MPC (open symbols), LF-MPC (full circles) and γ-NC/μ (stars+lines) obtained for different fluxes, the upper curve in dark blue corresponding to the highest flux. The dark Fermi level position is indicated by a vertical dashed line.

For instance, one can see that, though we have a good agreement in the CBT region for the HF-MPC and LF-MPC distributions, the DOS distribution found for the deep states from the LF-MPC data is about 7 times higher than the DOS distribution found from the HF-MPC results. Besides, in the 0.3 – 0.4 eV energy range the LF-MPC DOS could not be calculated because, in this region, the slope of tan(ϕ) was negative, as expected in the case of a material presenting sensitization behaviors [30].

We can also see that, despite the good agreement between the HF-MPC and LF-MPC in the CBT region, the γ-NC/μ distribution parallels the CBT but with values 20 to 25 times lower. At deeper energies the γ-NC/μ distribution extends up to the dark Fermi level where it drops abruptly. The reason is that, at high temperatures, the quasi Fermi level E_{Fn} tends towards E_{F0}. Finally, in the 0.3 – 0.4 eV energy range, the γ-NC/μ presents a minimum when calculated with the highest flux and could not be defined for the other fluxes, the γ values being larger than one, signature of a sensitization behavior.

Based on the theoretical developments exposed above, we can propose explanations for these discrepancies. For instance, we have shown in §2.2 that the C involved in the γ-NC/μ calculation is that of the main recombining states. At low temperatures only the band tails are predominant for recombination due to the large splitting of the quasi Fermi levels. As in the case of the numerical calculation presented in Fig. 2.2, we can assume that the C involved in the γ-NC/μ calculation is that of the VBT. Considering our theoretical results and comparing the experimental results of the HF-MPC and of SSPC, it means that the ratio C_n^{CBT}/C_n^{VBT} is of the order of 20-25 for the studied film. The fact that the capture coefficients for the CBT and VBT are quite different explains also the sensitization effect that results in γ values larger than one and the impossibility to plot the γ-NC/μ in the 0.3-0.4 eV range. Considering the deeper states, close to the Fermi level, there is a rather good agreement between the γ-NC/μ distribution and the HF-MPC-NC/μ. It means that the capture coefficients involved in each equation are probably very close.

If we compare the LF-MPC- and HF-MPC-NC/μ distributions in the range $0.55 \leq E_C - E \leq 0.7$ eV just above the Fermi level we can see a large discrepancy. Reminding that the LF-MPC technique gives the N value alone it means that the C/μ used to plot the LF-MPC-NC/μ was largely overestimated. It implies that, around the Fermi level, it exists a rather high defect distribution seen by the LF-MPC technique but with a low capture coefficient compared to that of the CBT, because these states are not really apparent on the HF-MPC NC/μ. We believe that these defects are amphoteric dangling bond (DB) states described by the defect-pool model [45], and the comparison of the HF-MPC-NC/μ and the LF-MPC NC/μ can give an order of magnitude of the ratio C_n^{pool}/C_n^{CBT}.

If we assume that the equivalent density of states in the conduction band of pm-Si:H is the same as that of crystalline silicon ($N_C \approx 2.5\times10^{19}$ cm^{-3}), we find the following values for some of the transport parameters: $C_n^{CBT} \approx 10^{-8}$ cm^{3}s^{-1} ; $N_{max}^{LF} \approx 6\times10^{17}$ cm^{-3}eV^{-1} ; $C_n^{VBT} \approx 5\times10^{-10}$ cm^{3}s^{-1} ; $C_n^{pool} \approx 8\times10^{-10}$ cm^{3}s^{-1} ; $\mu_n \approx 40$ cm^{2}V^{-1}s^{-1}. This mobility value is slightly higher than the one usually quoted in the literature ($\mu_n \approx 10$ cm^{2}V^{-1}s^{-1} [32]) but can be lowered by taking higher values for N_C.

Finally, there is still a discrepancy on the origin of which we can speculate. According to the LF-MPC distribution of states, there should exist a gap in between the deep states and the CBT states in the energy range 0.4-0.5 eV, whereas the HF-MPC present a continuously decreasing density of states. We suggest that, in this region, there exists a rather low defect density unseen by the LF-MPC technique (low N) but with a rather high capture coefficient responsible for the NC/μ values detected with the HF-MPC technique.

This speculation, and the values of the transport parameters, have been confirmed by numerical calculations. Introducing a density of states made of two band tails, a deep DB distribution and an extra Gaussian distribution of acceptor states, along with transport parameters the same order of magnitude as those found experimentally, we were able to calculate the HF-MPC-NC/μ, the LF-MPC-NC/μ and the γ-NC/μ, reproducing all the experimental features.

The DOS introduced in the calculation is presented in Fig. 2.14. It is made of two band tails, a distribution of deep DB defects, and a Gaussian distribution of acceptor states with a low maximum, $N_{max} = 10^{16}$ cm^{-3}eV^{-1} and a high capture coefficient $C_n^{Acc} = 10^{-7}$ cm^{3}s^{-1} in between the CBT and the deep DB states. The capture coefficients for the CBT, VBT, and deep DB states are displayed in the figure. The extended states mobilities were set at $\mu_n = 10$ cm^{2}V^{-1}s^{-1} and $\mu_p = 1$ cm^{2}V^{-1}s^{-1}. The LF-MPC-NC/μ was calculated with a DC flux of 3×10^{15} cm^{-2}s^{-1}, the HF-MPC-NC/μ with a DC flux of 10^{13} cm^{-2}s^{-1}, and the γ-NC/μ with these two fluxes. For more details on all the parameters introduced in the simulation the reader may refer to [60].

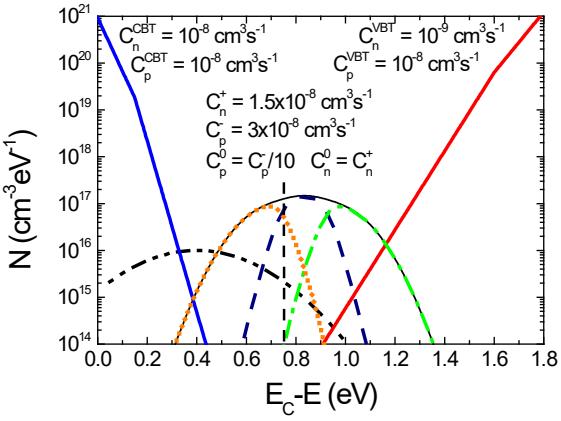

Fig. 2.14. DOS introduced in the numerical calculation including two band tails (red and blue lines), and a deep dangling bond defect distribution. The positively charged (D^+), neutral (D^0) and negatively charged (D^-) DB states are shown with dotted orange, dashed blue, and dash-dotted green lines, respectively. A Gaussian distribution of acceptor states (black dash-dot-dot line) is set in between the CBT and E_{F0}, displayed by a vertical dashed line.

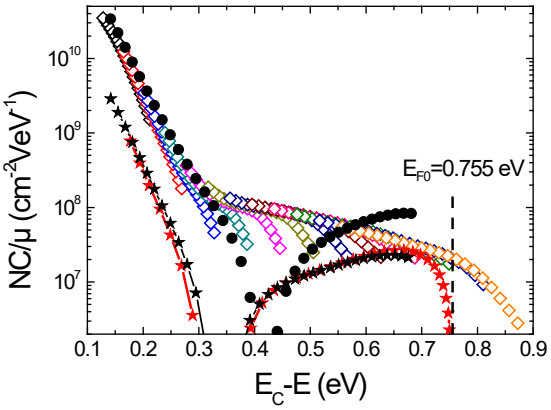

Fig. 2.15. Reconstructed NC/μ spectra from the simulation performed with the DOS of Fig. 2.14. The symbols are the same as in the experimental reconstruction of Fig. 2.13: HF-MPC (open diamonds), LF-MPC (full circles), γ-NC/μ (lines+stars). The position of the dark Fermi level is indicated by a vertical dashed line.

The results of the calculation in terms of reconstructed NC/μ spectra are presented in Fig. 2.15. To scale the energy we have chosen the same capture coefficient for all the techniques, as we did experimentally: the capture coefficient of the CBT. We did not plan to reproduce exactly the experimental results, but it can be seen that all the experimental features presented in Fig. 2.13 are well reproduced in Fig. 2.15. We are therefore confident in the fact that the combination of several techniques of characterization applied to the same material can bring excellent orders of magnitude of some of the transport parameters, as well as a model for the density of states distribution, a result that none of the considered techniques could have brought if performed alone.

2.4. Conclusion

The SSPC technique has been used for years as an easy way to estimate the photoconductive properties of a semiconductor. A power law dependence between the photoconductivity σ and the generation rate, $\sigma \propto G_{dc}^{\gamma}$, was sometimes noted and a link with the transport parameters of the material, for instance the carrier lifetime, was drawn in the early work of A. Rose. In this chapter, we have demonstrated that information on the semiconductor DOS can be extracted if one performs experiments at different fluxes and/or different temperatures using a generalized definition of the γ factor. We have presented a complete development from which, under simple assumptions, it is possible to achieve a DOS spectroscopy of the material by means of the SSPC technique. This theoretical development has been illustrated by means of numerical calculations. The experimental results of the SSPC technique have been compared to those of another characterization technique: the modulated photocurrent experiment. In this latter technique the flux of light is modulated at different frequencies and information on the DOS of the material is extracted from the modulus and the phase shift referred to the excitation of the resulting AC current. Two regimes have been put into evidence, the low frequency and the high frequency regime, and from each of them one can perform a DOS

spectroscopy of the material. A complete theoretical presentation of each of these regimes has been given, illustrated by some numerical calculations underlying the assumptions under which the MPC technique can be applied as well as its limitations. We have shown that the MPC technique in its high frequency regime can be applied to both intrinsic bulk crystalline and disordered thin film semiconductors. The transport parameters to which all these characterization techniques (SSPC, LF- and HF-MPC) are sensitive being not the same, one can take advantage of this property to extract as many transport parameters as possible. We have presented experimental results based on the application of the three techniques to the same thin film and shown that information can be obtained on the DOS as well as on the capture cross–sections of some states and on the carrier mobility. This last result underlines the necessity to use several characterization techniques to eventually estimate the largest set of transport parameters for a given material. It also underlines the powerfulness of the SSPC and MPC techniques.

Appendix: Notations used for the most important quantities (by alphabetic order)

C_n	Capture coefficient of a trap for electrons of the conduction band	(cm^3s^{-1})
C_p	Capture coefficient of a trap for holes of the valence band	(cm^3s^{-1})
d	Inter-electrode distance	(cm)
E	Energy of a state	(eV)
E_C	Energy of the bottom of the conduction band	(eV)
E_{Fn}	Quasi Fermi level for free electrons	(eV)
E_{F0}	Equilibrium Fermi level	(eV)
E^*_{F0}	Energy position symmetrical of E_{F0} with respect to mid gap	(eV)
E_g	Bandgap energy	(eV)
$e_n(E)$	Emission rate of an electron from a trap at E toward the conduction band	(s^{-1})
$e_p(E)$	Emission rate of a hole from a trap at E toward the valence band	(s^{-1})
E_{tn}	Quasi Fermi level for trapped electrons	(eV)
E_{tp}	Quasi Fermi level for trapped holes	(eV)
E_V	Energy of the top of the valence band	(eV)
$E_{\omega n}$	Energy defined by $e_n(E_{\omega n}) = \omega$	(eV)
$E_{\omega p}$	Energy defined by $e_p(E_{\omega p}) = \omega$	(eV)
F_{dc}	Direct component (DC) of the flux of light	($cm^{-2}s^{-1}$)
$f(E)$	Occupation function of a monovalent state at the energy E under light	
$f_0(E)$	Occupation function of a monovalent state at the energy E under dark	
$f_{ac}(E)$	Occupation function linked to the alternating component of the flux of light	
$f_{dc}(E)$	Occupation function linked to the direct component of the flux of light	
G	Generation rate	($cm^{-3}s^{-1}$)
G_{ac}	Alternating component (AC) of the generation rate	($cm^{-3}s^{-1}$)
G_{dc}	Direct component (DC) of the generation rate (Steady state)	($cm^{-3}s^{-1}$)
h	Planck constant	(4.136×10^{-15} eV s)
$h\nu$	Photon energy	(eV)
I_{ac}	Alternating component of the current flowing in the sample	(A)
I_{dc}	Direct component of the current flowing in the sample	(A)
$\vec{J}_n$	Electron current density	(A/cm^2)
$\vec{J}_p$	Hole current density	(A/cm^2)
k_B	Boltzmann constant	(8.617×10^{-5} eV K^{-1})

n	Free electron concentration under light	(cm^{-3})
n_{ac}	Alternating component of the free electron concentration due to the alternating generation	(cm^{-3})
n_{dc}	Direct component of the free electron concentration due to the steady generation	(cm^{-3})
n_0	Free electron concentration at equilibrium (in the dark)	(cm^{-3})
$N(E)$	Density of states at the energy E	($cm^{-3}eV^{-1}$)
N_C	Equivalent density of states at the bottom of the conduction band	(cm^{-3})
N_V	Equivalent density of states at the top of the valence band	(cm^{-3})
p	Free hole concentration under light	(cm^{-3})
p_{ac}	Alternating component of the free hole concentration due to the alternating generation	(cm^{-3})
p_{dc}	Direct component of the free hole concentration due to the direct generation	(cm^{-3})
p_0	Free hole concentration at equilibrium (in the dark)	(cm^{-3})
q	Absolute value of the electronic charge	(1.60×10^{-19} C)
S	Area through which the current is flowing	(cm^{-2})
t	Time	(s)
T	Temperature of the material	(K)
T_C	Characteristic temperature of the exponential conduction band tail	(K)
T_V	Characteristic temperature of the exponential valence band tail	(K)
α	Absorption coefficient	(cm^{-1})
γ	Gamma coefficient related to the dependence of photoconductivity upon generation rate	
Δn	Excess concentration of free electrons	(cm^{-3})
Δp	Excess concentration of free holes	(cm^{-3})
ε	Dielectric constant of the material	
ε_0	Vacuum permittivity	(8.854×10^{-14} F/cm)
μ_n	Extended states electron mobility	($cm^2V^{-1}s^{-1}$)
μ_p	Extended states hole mobility	($cm^2V^{-1}s^{-1}$)
ν	Frequency of the light	(Hz)
ν_n	Attempt-to-escape frequency of an electron trap	($\nu_n = C_nN_C$, s^{-1})
ν_p	Attempt-to-escape frequency of a hole trap	($\nu_p = C_pN_V$, s^{-1})
$\vec{\xi}$	Applied electric field	(Vcm^{-1})
σ	Photoconductivity of the material	(Scm^{-1})
τ_n	Electron lifetime	(s)
τ'_n	Lifetime of the excess electrons δn created by an excess generation δG	(s)
τ_p	Hole lifetime	(s)
τ'_p	Lifetime of the excess holes δp created by an excess generation δG	(s)
ϕ	Phase shift between the alternating current and the alternating generation rate	(radian)
ω	Angular frequency of the modulation of the light	(s^{-1})

Acknowledgements

We thank Pere Roca i Cabarrocas from the Laboratoire de Physique des Interfaces et Couches Minces (LPICM, Palaiseau, France) for the deposition of a-Si:H and pm-Si:H films.

We thank the SOLSIA company for providing some of the a-Si:H samples in the framework of the POLYSIL project funded by the Agence de l'Environnement et de la Maîtrise de l'Energie (ADEME)

Thanks also to Pawel Kaminski from Institute of Electronic Materials Technology (ITME, Warsaw, Poland) for providing the GaAs:Cr samples in the framework of Polonium project 7023.

Part of this work was carried out under Ecos-Sud projects A02E01, A08E01, and A13E02.

References

1 Bube, R. H. (1960) "*Photoconductivity of Solids*", Wiley, New York.
2 Bube, R. H. (1992) "*Photoelectronic Properties of Semiconductors*", Cambridge University Press, Cambridge.
3 Ryvkin, S. M. (1964) "*Photoelectric Effects in Semiconductors*", Consultants Bureau, New York.
4 Rose, A. (1966) "*Concepts in photoconductivity and allied problems*", Wiley & Sons, New York.
5 Reynolds, S., Brinza, M., Benkhedir, M. L., Adriaenssens, G. J. (2017) "*Photoconductivity in materials research*", in "Springer Handbook of Electronic and Photonic Materials", edited by S. Kasap, P. Capper, Springer International Publishing AG.
6 Abe, K., Okamoto, H., Nitta, Y., Tsutsumi, Y., Hattori, K., Hamakawa, Y. (1988) *Philos. Mag. B* 58: 171.
7 Vaněček, M., Kocka, J., Stuchlik, J., Triska, A. (1981) *Solid State Comm.* 39: 1199.
8 Antoniadis, H., Schiff, E. A. (1992) *Phys. Rev. B* 46: 9482.
9 Main, C. (1997) *Mat. Res. Soc. Proc.* 467: 167.
10 Hurtes, Ch., Boulou, M., Mitonneau, M., Bois, D. (1978) *Appl. Phys. Lett.* 32: 821.
11 Oheda, H. (1981) *J. Appl. Phys.* 52: 6693.
12 Ritter, D., Zeldov, E., Weiser, K. (1986) *Appl. Phys. Lett.* 49: 791.
13 Ritter, D., Weiser, K., Zeldov, E. (1987) *J. Appl. Phys.* 62: 4563.
14 Hattori, K., Koji, Y., Fukuda, S., Ma, W., Okamoto, H. (1993) *J. Appl. Phys.* 73: 3846.
15 Poruba, A., Vanecek, M., Rosa, J., Feitknecht, L., Wyrsch, N., Meier, J., Shah, A., Repmann, T., Rech, B. (2001) in *Proceedings of the 17th European Photovoltaic Solar Energy Conference* (WIP, Munich, Germany), 2981.
16 Vaněček, M., Poruba, A. (2002) *Appl. Phys. Lett.* 80: 719.
17 Tsutsumi, Y., Sakata, S., Abe, K., Nitta, Y., Okamoto, H., Hamakawa, Y. (1987) *J. Non-Cryst Solids* 97-98: 1063-1066.
18 Djebbour, Z., Serhan, J., Migan-Dubois, A., Mencaraglia, D. (2010) *J. Appl. Phys.* 108: 043707.
19 Haken, U., Hundhausen, M., Ley, L. (1993) *Appl. Phys. Lett.* 63: 3066.
20 Haken, U., Hundhausen, M., Ley, L. (1995) *Phys. Rev. B* 51: 10579.
21 Ventosinos, F., Budini, N., Longeaud C., Schmidt, J. A. (2011) *J. Phys. D: Appl. Phys.* 44: 295103.
22 Longeaud, C., Ventosinos, F., Schmidt, J. A. (2012) *J. Appl. Phys.* 112: 023709.
23 DeOSt software https://www.geeps.centralesupelec.fr/index.php?page=en-pv_deost
24 Liu, J. Z., Wagner, S. (1989) *Phys. Rev. B* 39: 11156.
25 Mendoza, D., Pickin, W. (1989) *Phys. Rev. B* 40: 3914.
26 Tran, M. Q. (1995) *Philos. Mag. B* 72: 35.
27 Shen, D. S., Wagner, S. (1995) *J. Appl. Phys.* 78: 278.
28 Simmons, J. G., Taylor, G. W. (1971) *Phys. Rev. B* 4: 502.
29 Taylor, G. W, Simmons, J, G. (1972) *J. Non-Cryst. Solids* 8-10: 940.
30 Schmidt, J. A., Longeaud, C., Koropecki, R. R., Arce, R. D. (2007) *J. Appl. Phys.* 101: 103705-1-10.
31 Longeaud, C., Schmidt, J. A., Kleider, J. P. (2006) *Phys. Rev. B* 73: 235316.
32 Tiedje, T. (1984) in "*Semiconductors and Semimetal 21C*", edited by J. Pankove, Academic Press, New York: pp 207-238.
33 Stutzmann, M. (1989) *Philos. Mag. B* 60: 531.
34 Winner, K., Ley, L. (1989) in "*Amorphous semiconductors and related materials*", edited by H. Fritzsche, World Scientific, Singapore: 365.
35 Brüggemann, R., Main, C., Berkin, J., Reynolds, S. (1990) *Philos. Mag. B* 62: 29.
36 Longeaud, C., Kleider, J. P. (1992) *Phys. Rev. B* 45: 11672.
37 Kleider, J. P., Longeaud, C. (1995) in Solid State Phenomena, edited by H. Neber-Aeschbacher (Scitec Publications Ltd.) pp 597-646.

38 Shockley, W., Read, W. T. (1952) *Phys. Rev.* 87: 835.
39 Hall, R. N. (1951) *Phys. Rev.* 83: 228.
40 Hall, R. N. (1952) *Phys. Rev.* 87: 387.
41 Gueunier, M. E., Longeaud, C., Kleider, J. P. (2004) *Eur. Phys. J. Appl. Phys.* 26: 75.
42 Koropecki, R. R., Schmidt, J. A., Arce, R. (2002) *J. Appl. Phys.* 91: 8965.
43 Kounavis, P. (2001) *Phys. Rev. B* 64: 45204.
44 Lachaume, R., Longeaud, C., Kleider, J. P. (2016) *Phys. Status Solidi* A 213: 1848.
45 Powell, M. J., Deane, S. C. (1993) *Phys. Rev. B* 48: 10815.
46 Longeaud, C., Kleider, J. P. (1993) *Phys Rev. B* 48: 8715.
47 Longeaud, C., Kleider, J. P., Mencaraglia, D., Amaral, A., Carvalho, C. N. (1993) *J. Non-Cryst. Solids* 164-166: 423-426.
48 Kleider, J. P., Longeaud, C., Meaudre, R., Meaudre, M., Vignoli, S., Koughia, K. V., Terukov, E. I., Konkov, O. I. (2001) *Mat. Science and Engineering* B81: 71–73.
49 Luckas, J., Longeaud, C., Bertram, T., Siebentritt, S. (2014) *Appl. Phys. Lett.* 104: 153905.
50 Krysztopa, A., Igalson, M., Aida, M., Larsen, J. K., Gütay, L., Siebentritt, S. *J. Appl. Phys.* 110: 103711.
51 Darga, A., Mencaraglia, D., Longeaud, C., Savenije, T. J., O'Regan, B., Bourdais, S., Muto, T., Delatouche, B., Dennler, G. (2013) *J. Phys. Chem. C* 117: 20525.
52 Longeaud, C., Luckas, J., Krebs, D., Carius, R., Klomfass, J., Wuttig, M. (2012) *J. Appl. Phys.* 112: 113714.
53 Luckas, J., Piarristeguy, A., Bruns, G., Jost, P., Grothe, S., Schmidt, R. M., Longeaud, C., Wuttig, M., (2013) *J. Appl. Phys.* 113: 023704.
54 Frejlich, J., Montenegro, R., Inocente-Junior, N. R., dos Santos, P. V., Launay, J. C., Longeaud, C., Carvalho, J. F. (2007) *J. Appl. Phys.* 101: 043101.
55 Verstraeten, D., Longeaud, C., BenMahmoud, A., von Bardeleben., H. J., Launay, J. C., Viraphong, O., Lemaire, Ph. C. (2003) *Semicond. Sci. Technol.* 18: 919–926.
56 Longeaud, C., Kleider, J. P., Kaminski, P., Kozlowski, R., Pawlowski, M., Cwirko, J. (1999) *Semicond. Sci. Technol*. 14: 747–756.
57 Longeaud, C., Kleider, J. P., Kaminski, P., Kozlowski, R., Miczuga, M. (2009) *J. Phys.: Condens. Matter* 21: 045801.
58 Bourgoin, J. C., von Bardeleben, H. J., Stievenard, D. (1988) *J. Appl. Phys.* 64: R 65.
59 Yasutake, K., Kakiuchi, H., Takeuchi, H., Yoshi, A., Kawabe, H. (1997) *J. Mater. Sci.: Materials in electronics* 8: 239.
60 Longeaud, C., Schmidt, J. A., Koropecki, R. R. (2006) *Phys. Rev. B* 73: 235317.